

Energy Advances

Accepted Manuscript

This article can be cited before page numbers have been issued, to do this please use: P. Tzevelekidis, E. Sakellis, L. Koutsokeras, O. Martzoukou, N. Boukos and C. A. Mitsopoulou, *Energy Adv.*, 2026, DOI: 10.1039/D5YA00313J.



This is an Accepted Manuscript, which has been through the Royal Society of Chemistry peer review process and has been accepted for publication.

Accepted Manuscripts are published online shortly after acceptance, before technical editing, formatting and proof reading. Using this free service, authors can make their results available to the community, in citable form, before we publish the edited article. We will replace this Accepted Manuscript with the edited and formatted Advance Article as soon as it is available.

You can find more information about Accepted Manuscripts in the [Information for Authors](#).

Please note that technical editing may introduce minor changes to the text and/or graphics, which may alter content. The journal's standard [Terms & Conditions](#) and the [Ethical guidelines](#) still apply. In no event shall the Royal Society of Chemistry be held responsible for any errors or omissions in this Accepted Manuscript or any consequences arising from the use of any information it contains.

1 Highly active Cu-Freudenbergite/TiO₂ 2 heterojunction for solar-driven hydrogen 3 evolution and 5-hydroxymethylfurfural oxidation

4 *Panagiotis Tzevelekidis,^a Elias Sakellis,^{b,c} Loukas Koutsokeras,^c Olga Martzoukou,^d Nikos
5 Boukos,^b and Christina A. Mitsopoulou^{*a}*

6 ^a Inorganic Chemistry Laboratory, Department of Chemistry, National and Kapodistrian University
7 of Athens 15771 Zografou, Greece

8 ^b Institute of Nanoscience and Nanotechnology, National Centre of Scientific Research
9 "Demokritos", Agia Paraskevi, 15341, Greece

10 ^c Section of Condensed Matter Physics, Department of Physics, National and Kapodistrian
11 University of Athens, Athens, 15784, Greece

12 ^d Enzyme and Microbial Biotechnology Unit, Department of Biology, National and Kapodistrian
13 University of Athens, Athens, 15784, Greece

14 * To whom correspondence should be addressed: cmtsop@chem.uoa.gr

15 Abstract

16 The pursuit of efficient photocatalytic systems for solar light-driven hydrogen evolution (HER) drives the
17 search for novel semiconductor materials capable of forming advanced heterojunctions. Herein, we report
18 the first synthesis of a non-stoichiometric, Cu-substituted freudenbergite (Cu-FDT) via a facile co-
19 precipitation method. Comprehensive characterization (PXRD, XPS, RAMAN, HR-TEM/STEM-EDS)
20 confirms the formation of a phase-pure freudenbergite structure with nanoplatelet morphology and mixed-
21 valent Ti⁴⁺/Ti³⁺. Electronic characterization (UV-DRS, Mott-Schottky) reveals a bandgap (E_g) value of 2.95
22 eV enabling extended solar light harvesting and a band alignment perfectly suited for HER, coupled with a
23 strong oxidation potential for the valence band (VB). A modified synthetic approach, involving the addition
24 of water during Cu-FDT peptization, enabled the *in situ* fabrication of a Cu-FDT/TiO₂ heterojunction. The
25 TiO₂ phase (anatase, mixed phase, rutile) was tuned by varying the calcination temperature. Photocatalytic
26 performance toward HER was evaluated for all composites to elucidate the effect of excess surface Na⁺ on
27 photocatalytic activity. The optimal catalyst, a 1 wt% Pt-loaded, desodiated Cu-FDT/anatase heterojunction
28 (1 wt% Pt @ Cu-FDT_A deNa), achieved a high hydrogen production rate of 7183 μmol ·g⁻¹·h⁻¹ under solar
29 irradiation. To correlate electrochemical properties with HER performance, EIS, photocurrent density, and
30 LSV measurements toward the HER were conducted on anatase TiO₂, Cu-FDT and their heterojunction,
31 comparing Na⁺-rich and desodiated surfaces. Mott-Schottky analysis confirmed a direct Z-scheme charge
32 transfer mechanism, enabling superior charge separation while preserving strong redox potentials.
33 Furthermore, the high oxidative power of the heterojunction was further demonstrated by the near-complete
34 mineralization of 5-hydroxymethyl furfural (5-HMF), with only minimal yields of partial oxidation
35 products 5-hydroxymethyl-2-furancarboxylic acid (HMFCA) and 2,5-diformylfuran (DFF). These findings
36 highlight the potential of this novel photocatalyst to simultaneously drive HER and challenging oxidation



37 reactions, thus coupling renewable H₂ evolution with the potent oxidative power of photogenerated holes
38 (h⁺) in the VB of Cu-FDT.

39

40 **Keywords:** Photocatalysis; Hydrogen Evolution Reaction (HER); Cu-substituted Freudenbergite;
41 Z-scheme Heterojunction; 5-Hydroxymethylfurfural Oxidation

42 1. Introduction

43 Depletion of fossil fuels and the resulting impact on Earth's climate and the global
44 economy have shifted the attention to the pursuit of renewable energy sources with zero carbon
45 emissions.¹ Solar-driven photocatalysis and especially water splitting into H₂ and O₂, represents a
46 promising pathway for sustainable energy conversion as H₂ energy content far surpasses the energy
47 obtained from the combustion of fossil fuels.² However, major drawbacks of this process include
48 the low utilization of the full potential of photocatalysts due to rapid electron (e⁻)-hole(h⁺)
49 recombination and the sluggish reaction kinetics of the oxygen evolution reaction (OER).³
50 Titanium dioxide (TiO₂) has been widely studied as a benchmark photocatalyst due to its robust
51 stability, low cost, and favorable band positions for both the hydrogen evolution reaction (HER)
52 and the OER. Nevertheless, certain limitations such as the large band gap (3.2 eV) of anatase - the
53 most photocatalytic active phase of TiO₂ - which in turn restricts its use in the UV region, as well
54 as the inherent fast charge recombination, hinder practical application.^{4,5}

55 Several approaches have been employed to overcome the limitations of TiO₂, including
56 doping with transition metals (e.g., Fe, Cu, Ni) to create mid-gap states and extend the light
57 absorption into the visible-light region, as well as anionic doping (e.g., N, S).⁶⁻¹⁰ Furthermore,
58 decoration with noble metal nanoparticles (e.g., Au, Ag, Pd) has been employed to exploit the
59 surface plasmon resonance (SPR) effect, which enhances light harvesting and promotes charge
60 separation.^{6,11} Another well-established strategy is the addition of co-catalysts such as Cu and Pt
61 for HER, since they serve as electron sinks, that efficiently collect photogenerated electrons from
62 the TiO₂ light-harvesting support and facilitating the reduction of protons (H⁺) to H₂.¹²⁻¹⁴

63 Constructing heterojunctions between TiO₂ and other semiconductors is an effective
64 alternative strategy, proven to enhance charge separation through Type II, Z- and S-scheme charge
65 transfer. Many semiconductors have been used in heterojunctions with anatase TiO₂, such as g-
66 C₃N₄, CdS, ZnIn₂S₄, and others, known for creating efficient heterojunctions and exhibiting
67 notable activities for H₂ generation under solar-light irradiation.¹⁵⁻¹⁷ In this context, the
68 combination of TiO₂ with other TiO₂ polymorphs like rutile, brookite and TiO₂(B) and perovskites
69 has emerged as a powerful strategy for developing efficient heterojunction systems, as strong
70 interfacial bonding and optimal band alignment with anatase significantly enhances charge
71 separation.¹⁸⁻²¹ Recent work on Cu- and Ni-doped Na₂Ti₆O₁₃ and Na₂Ti₃O₇ has shown that
72 transition-metal incorporation can tune the band structure and electrical conductivity of tunnel
73 titanates, suggesting a viable route toward visible-light-responsive, mixed-valence Ti³⁺ systems.²²⁻²⁴

75 Freudenbergite, Na₂Fe³⁺₂Ti₆O₁₆, is a less-explored titanium-based material that offers a
76 compelling partner for forming such heterojunctions. First identified by Frenzel in 1958 and later

77 structurally characterized by Ishiguro *et al.* in 1978, it exhibits a titanate-like structure and a
78 monoclinic space group (C2/m) consisting of TiO_6 octahedra forming tunnels that accommodate
79 charge balancing cations like Na^+ .^{25,26} Notably, this structure allows substantial cationic
80 substitution with transition metals on the Ti^{4+} sites, which significantly narrows the bandgap and
81 enhances visible-light absorption.^{27,28} Recent reports on Na-Mg-Fe-Ti-O solid solutions confirm
82 the compositional flexibility and photoactive potential of these freudenbergite-type lattices^{29,30}
83 Ciocarlan *et al.* reported a heterojunction of Freudenbergite with Zn-Ni ferrite which demonstrated
84 exceptional efficiency in organic dye degradation (Methylene Blue and Rhodamine G) under
85 visible-light irradiation owing to the small band gap of ferrite and $\text{FeNaTi}_3\text{O}_8$ Freudenbergite (~2.2
86 eV), as well as due to the strong adsorption properties of $\text{FeNaTi}_3\text{O}_8$.³¹ The electronic properties
87 of transition metal-substituted freudenbergites make them particularly attractive for photocatalytic
88 applications as the band structure of $\text{FeNaTi}_3\text{O}_8$ creates a sufficiently positive valence band (VB)
89 position for strong oxidative activity while maintaining a sufficient reductive conduction band
90 (CB) for H_2O reduction, while the presence of mixed valence states ($\text{Ti}^{4+}/\text{Ti}^{3+}$ and $\text{Fe}^{3+}/\text{Fe}^{2+}$) further
91 enhances carrier dynamics.^{31–33}

92 Despite these promising findings, no study has yet reported the substitution of Fe by Cu
93 within the Freudenbergite lattice, nor the coexistence of Ti^{3+} species stabilized through this
94 substitution. Such substitution is expected to include unique electronic perturbations due to the
95 redox flexibility of $\text{Cu}^{2+}/\text{Cu}^{1+}$ and its strong interaction with Ti^{3+} sites, which may synergistically
96 enhance charge-transfer and improve photocatalytic activity.

97 The implementation of efficient overall water splitting systems remains a formidable
98 challenge, primarily due to the thermodynamically demanding OER. To overcome this bottleneck,
99 a common strategy employs sacrificial electron donors such as triethanolamine (TEOA) or
100 methanol (MeOH), which act as h^+ scavengers. The rapid consumption of h^+ suppresses e^- - h^+
101 recombination, thereby increasing the lifetime of e^- available for HER.³⁴ In this context, the
102 photocatalytic oxidation and reforming of biomass-derived substrates has emerged as a promising
103 alternative strategy.³⁵ 5-Hydroxymethylfurfural (5-HMF) is a pivotal, biomass-derived platform
104 molecule that serves as a versatile precursor for a wide range of valuable chemicals. Its structure
105 comprises a furan ring with aldehyde and hydroxymethyl functional groups that allow for selective
106 oxidation into high-value products, such as 2,5-furandicarboxylic acid (FDCA), 2,5-diformylfuran
107 (DFF) and 5-hydroxymethyl-2-furancarboxylic acid (HMFCA).³⁶ The photocatalytic oxidation of
108 5-HMF offers a sustainable approach to replace classic electron donors and recent studies have
109 demonstrated the photocatalytic selective conversion of 5-HMF to value added chemicals coupled
110 with H_2 generation using heterojunctions of semiconductor materials such as $\text{g-C}_3\text{N}_4$, TiO_2 , In_2O_3
111 and ZnIn_2S_4 .^{37–39}

112 Herein, to the best of our knowledge, we report for the first time the synthesis of a Cu-
113 substituted Freudenbergite (Cu-FDT), via a facile co-precipitation route, leading to the
114 stabilization of mixed-valence $\text{Ti}^{3+}/\text{Ti}^{4+}$ - Cu^{2+} sites. The resulting material was comprehensively
115 characterized: its structure and morphology were elucidated by PXRD, XPS, Raman, HR-TEM
116 and STEM-EDS, while its electronic properties were determined using UV-DRS and Mott-
117 Schottky analysis. Notably, we discovered that introducing a minimal quantity of water during Cu-
118 FDT synthesis facilitated the *in-situ* formation of a heterojunction between Cu-FDT and anatase
119 TiO_2 . This *in situ* formation is a key advantage for heterojunction formation, ensuring optima



120 interfacial contact. The phase composition and stability of this composite were further examined,
121 revealing that the TiO_2 polymorph and Cu-FDT content could be precisely tuned by varying the
122 calcination temperature. The photocatalytic performance of these heterojunctions was evaluated
123 for solar driven HER before and after the removal of excess surface sodium. The most active
124 catalyst—namely, the 1 wt% Pt-loaded, desodiated CuFDT/anatase heterojunction (1 wt% Pt @ Cu-
125 FDT_A deNa), exhibited outstanding performance, achieving a remarkable HER activity of 7183
126 $\mu\text{molH}_2 \cdot \text{g}^{-1} \cdot \text{h}^{-1}$ using TEOA as a sacrificial electron donor. Electrochemical measurements (EIS,
127 photocurrent density, LSV) confirmed enhanced activity for HER in both Na^+ -rich and desodiated
128 Cu-FDT/anatase heterojunctions. The superior photocatalytic performance of the desodiated
129 photocatalysts is attributed primarily to improved surface properties that favor Pt co-catalyst
130 loading and H_2O reduction. Mott-Schottky analysis of the optimal composite revealed the
131 formation of a heterojunction with Fermi-band position pointing to a direct Z-scheme charge
132 transfer mechanism at the Cu-FDT/anatase interface, which accounts for the superior spatial
133 separation of photogenerated charge carriers while preserving the strong redox potential necessary
134 to drive catalytic reactions. Finally, we demonstrated the practical oxidative capability of the
135 heterojunction through the photocatalytic oxidation of the biomass-derived platform chemical, 5-
136 HMF. The reaction pathway proceeded predominantly via deep oxidation of 5-HMF with only
137 limited quantities of partial oxidation intermediates, HMFCA and DFF, being detected. This
138 observation underscores the potent oxidative power of photogenerated h^+ residing in the VB of
139 Cu-FDT, which drives the photooxidation of 5-HMF.
140

141 2. Experimental section

142 2.1 Materials

143 Titanium(IV) *i*-propoxide TTIP (97%), Absolute ethanol – EtOH (99.8%), Methanol – MeOH
144 (99%), Acetone – AcON (99%), Copper(II) nitrate trihydrate – $\text{Cu}(\text{NO}_3)_2 \cdot 3\text{H}_2\text{O}$ (99%),
145 Anhydrous acetic acid – AA (99.8%), Acetonitrile – MeCN, (99%) Sodium hydroxide – NaOH
146 pellets, HCl (37%) and Triethanolamine – TEOA (98%) were purchased from Acros Organics
147 and used without further purification. 5-hydroxymethyl furfural – 5-HMF (98%) was purchased
148 from Sigma-Aldrich. Barium sulfate – BaSO_4 (99%) and Potassium tetrachloro-platinate – K_2PtCl_4
149 were obtained from Thermo Fisher Scientific. Nafion was obtained from Sigma-Aldrich. A
150 Rephile Milli-Q system provided Ultra-pure water (MilliQ H_2O) which was used for all the
151 synthetic and experimental procedures. Argon – Ar (99%), Nitrogen – N₂ (99.7%) gasses and
152 compressed air were supplied by Revival N.C.

153 2.2 Photocatalyst preparation

154 2.2.1 Cu-Freudenbergite (Cu-FDT)

155 Cu-FDT was synthesized via a co-precipitation method. Specifically, 1.53 ml (0.005 mol) TTIP
156 was added dropwise, under continuous stirring to 10 ml of deaerated, Ar-saturated EtOH in a round
157 bottom flask. Subsequently, 0.48 ml (0.008 mol) of AA were added to initiate hydrolysis and
158 coordination with Ti (IV). The solution was stirred for 1 h in the dark and at 25°C, after which a 3



159 mol% Cu(²⁺) equivalent (relative to Ti(⁴⁺)) was added in the form of Cu(NO₃)₂ · 3H₂O dissolved in
160 1 ml EtOH. The resulting homogenous light blue solution was kept in the dark under constant
161 stirring for an additional 1 hour. Next, 4 ml of a 2 M NaOH solution (Na/Ti molar ratio= 1.6) was
162 rapidly injected causing the mixture to immediately turn opaque. Over the following hour the
163 dispersion transformed into a light blue, highly viscous gel. The gel was subjected to
164 ultrasonication for 1 h in 5 ml AcON and after vacuum drying, the obtained powder was washed
165 repeatedly with ethanol to remove unreacted precursors and then calcined at 550 °C for 4 h (heating
166 rate: 10°C/min) to yield the final product. Pure TiO₂ anatase was synthesized following the same
167 experimental procedure, without the addition of Cu precursor and used for the Mott-Schottky
168 experiments.

169 2.2.2 Cu-FDT/TiO₂ heterojunction

170 Heterojunctions of Cu-FDT with different TiO₂ were synthesized *in situ* following the same
171 synthetic procedure, but with an additional step of introducing minimal amount of MilliQ H₂O
172 before the introduction of NaOH. Specifically, to the mixture of TTIP, Cu(NO₃)₂ · 3H₂O and AA
173 in the ratios mentioned in 2.2.1, 100 µl of H₂O were added, causing the solution to turn colourless
174 but without any precipitation being observed. The rest of the synthetic procedure remained the
175 same and the resulting powder obtained after vacuum drying was washed repeatedly with ethanol
176 and water and calcined at 550°C (4h), 650°C (4h), 750°C (4h), and 850°C (4h). The final samples
177 were finely ground and denoted as Cu-FDT_A, Cu-FDT_B, Cu-FDT_C, Cu-FDT_D.

178 2.2.3 Desodiation of the photocatalysts

179 Another set of catalysts was prepared by removing excess Na⁺ ions from the catalytic surface.
180 Following the synthetic and cleaning procedures in 2.2.2, the photocatalyst powders were
181 dispersed in 200 ml of a 1 M HCl solution at a concentration of 1 mg/ml and subjected to ultrasound
182 treatment for 2 h to ensure thorough desodiation. Subsequently, the photocatalysts underwent
183 rigorous washing with MilliQ H₂O to eliminate residual NaCl, until the pH of the supernatant
184 reached 6.8 - 7. The desodiated powders were then subjected to calcination under the same
185 conditions as previously described in 2.2.2. The resulting photocatalysts, calcined at 550°C (4h),
186 650°C (4h), 750°C (4h), and 850°C (4h) were denoted as Cu-FDT_A deNa, Cu-FDT_B deNa, Cu-
187 FDT_C deNa, Cu-FDT_D deNa.

188 2.2.4 Pt photodeposition

189 Photodeposition of the Pt co-catalyst for the hydrogen evolution reaction was conducted as
190 follows: 20 mg of the photocatalyst were dispersed in a 50% (v/v) aqueous MeOH solution within
191 a glass reactor. A stoichiometric amount of K₂PtCl₆ was added to achieve 1 wt% Pt loading. The
192 suspension was saturated with Ar for 30 min, to ensure an O₂-free environment. Photodeposition
193 was carried out under UV-visible irradiation ($\lambda > 300$ nm) using a 300 W Xe solar simulator
194 (Quantum Design, LSH302) equipped with an AM 1.5 G filter. After 2 h of irradiation, the Pt-
195 loaded photocatalyst was recovered by centrifugation, thoroughly washed with MilliQ H₂O, and
196 dried at 80°C for 12 h.

197 2.3 Structural and optical characterization



198 Powder X-ray diffraction was carried out in a Bruker D8 Advance diffractometer, operated in
199 Bragg-Brentano geometry, at 40 kV and 25 mA. The X-ray source was a Cu anode with $\lambda = 1.5418$
200 \AA for the $\text{K}\alpha_1$. The diffraction patterns were recorded for $10 - 85 2\theta$ with step size of $0.02^\circ 2\theta/\text{s}$
201 and step duration at 0.22 s. Crystal phase indexing, crystallinity evaluation and relative percentages
202 of the crystalline phases at each sample were performed using Diffrac. EVA software. Rietveld
203 refinement was performed utilizing Profex software. The average crystallite size was calculated
204 for the (020) crystal plane of Cu-FDT at 47.5° employing the Scherrer equation:

$$205 D = \frac{k\lambda}{\beta(2\theta) \cos\theta} \quad (1)$$

206 where D represents the crystallite size, k is the shape factor, λ refers to the wavelength of the X-
207 rays, θ is the Bragg angle and $\beta(2\theta)$ corresponds to the line broadening at full width at half-
208 maximum (FWHM) of the (411) diffraction. For the PXRD analysis of Cu-FDT, the diffraction
209 pattern was recorded for $3 - 85 2\theta$, with a step size of $0.03^\circ 2\theta/\text{s}$ and step duration of 5 s, to ensure
210 high data quality for the Rietveld Refinement.

211 Raman analysis of the synthesized photocatalysts was conducted on a dual-source micro-Raman
212 inVia Qontor spectrometer from Renishaw with the use of the 785 nm Ar laser beamline.
213 The X-ray photoelectron spectroscopy (XPS) experiments were carried out in an ultra-high
214 vacuum system (UHV) equipped with an X-Ray gun. Unmonochromatized $\text{MgK}\alpha$ line at 1253.6
215 eV and two analyzer pass energies of 15 eV (giving a full width at half maximum (FWHM) of 0.85
216 eV for the $\text{Ag 3d}_{5/2}$ peak) and 40 eV were used. The XPS core level spectra were analyzed using a
217 fitting routine, which can decompose each spectrum into individual mixed Gaussian-Lorentzian
218 peaks after a Shirley background subtraction. Errors in our quantitative data are found in the range
219 of $\sim 10\%$, (peak areas) while the accuracy for BEs assignments is ~ 0.1 eV. The samples were in
220 powder form and pressed onto In foil while the analyzed area was a rectangle of $7.0 \times 15\text{mm}^2$.
221 FT-IR spectroscopy was conducted on a Shimadzu IRAffinity spectrometer bearing an ATR
222 (attenuated total reflection) QATR10 single-reflection accessory. Spectra were recorded in the
223 range of $400 - 4000 \text{ cm}^{-1}$.

224 UV-DRS absorbance and reflectance spectra were recorded on a Shimadzu UV-260
225 spectrophotometer bearing an integrating sphere attachment (ISR-2600Plus) with BaSO_4
226 employed as reference. Catalyst powder and BaSO_4 were mixed in a ratio of 1:10, finely ground
227 to create a homogenous mixture, and thinly pressed on the sample holder. Reflectance data were
228 transformed into Kubelka-Munk plots for the calculation of the indirect bandgap of the
229 semiconductors by plotting $(F(R_\square)hv)^{1/2}$ versus the photon energy. Extrapolation of the linear part
230 below the direct transition to the x-axis intercept gave the value of the indirect bandgap.
231 PL spectra were acquired with a Horiba Jobin-Yvon iHR320 spectrofluorometer using an
232 excitation wavelength of 310 nm for all measurements.



233 Transmission electron microscopy (TEM) and scanning transmission electron microscopy
234 (STEM) was conducted using a Talos F200i field-emission scanning transmission electron
235 microscope (Thermo Fisher Scientific, Waltham, MA), operating at an acceleration voltage of 200
236 kV and integrated with a Bruker 6T/100 windowless energy-dispersive X-ray spectroscopy
237 (EDAX) system (Hamburg, Germany). Ethanolic dispersions of catalyst samples were deposited
238 onto nickel TEM grids via drop-casting for imaging. Quantitative size analysis was performed by
239 statistically evaluating approximately 80 distinct nanoparticles using ImageJ processing software.
240 SEM (scanning electron microscopy) images were collected with a Quanta Inspect Microscope
241 from FEI operating at 15-25 keV.

242

243 *2.4 Electrochemical measurements*

244 Photoelectrochemical and electrochemical measurements were performed using a standard three-
245 electrode configuration with a VersaSTAT 3 Potentiostat/Galvanostat (AMETEK, Inc., USA),
246 controlled by VersaSTAT software for data acquisition and analysis. For transient photocurrent
247 and electrochemical impedance (EIS) measurements, the working electrode was prepared by drop-
248 casting a catalyst ink onto an FTO glass substrate (1 cm x 1 cm). The ink was prepared by
249 dispersing 5 mg of powder in 1 ml of 20% v/v Nafion ethanolic solution, followed by
250 ultrasonication for 30 minutes and overnight drying at 60 °C. A Pt wire and an Ag/AgCl (saturated
251 KCl) electrode served as the counter and reference electrodes, respectively, with a 0.2 M Na₂SO₄
252 aqueous solution as the electrolyte. Photocurrent density versus time (I-t) curves were recorded
253 using chronoamperometry at a constant bias of 0.5 V vs. Ag/AgCl under chopped illumination
254 from a 300 W Xe lamp, using light on/off cycles of 20 seconds each. EIS was conducted at the
255 open-circuit potential at the frequency range of 10 kHz to 0.01 Hz with an AC amplitude of 5 mV.
256 For linear sweep voltammetry (LSV) measurements related to HER activity, the working electrode
257 was prepared similarly by drop-casting the same catalyst ink onto a 1 cm x 1 cm carbon paper
258 substrate. The 0.5 M H₂SO₄ solution which served as the electrolyte for HER was thoroughly
259 deaerated for 30 min with Ar flow. LSV was carried out with a scan rate of 5 mV/s, and all
260 polarization curves were iR corrected. The measured potentials were calibrated to the Reversible
261 Hydrogen Electrode (RHE) scale using the following relation:

$$262 E_{vs. RHE} = E_{vs. Ag/AgCl} + 0.059 \times pH + 0.197 V \quad (2)$$

263 The Tafel slope was subsequently derived from the linear region of the corresponding Tafel plot.
264 For the Mott-Schottky analysis, the working electrode was prepared by dispersing 5 mg of the
265 photocatalyst in 50 µl of a 20% v/v Nafion solution in EtOH, followed by 5 mins of ultrasonication
266 to ensure homogeneity. The resulting ink was drop-cast onto a polished glassy carbon electrode
267 (0.071 cm² surface area) and dried overnight at RT. Measurements were using the same counter
268 and reference electrodes, and a 2 M KCl aqueous electrolyte solution. The Mott-Schottky plots



269 were obtained at 1000 and 5000 Hz with a DC potential sweep from 0.3 to -1 V, under dark
270 conditions, to assess the flat-band potential of the semiconductor photocatalyst.
271 For the determination of the relative band edge positions of Cu-FDT and TiO₂ anatase
272 heterojunction components, a combined UV-DRS and Mott-Schottky analysis was employed. The
273 flat-band potential obtained from Mott-Schottky measurements were used to approximate the CB
274 edge positions of the n-type semiconductors, while the VB positions were subsequently derived
275 from UV-DRS according to the following relation:

276

$$277 E_{VB} = E_{CB} + E_g \quad (3)$$

278 Where E_{VB} and E_{CB} represent the VB and CB edge positions respectively, and E_g is the bandgap
279 energy obtained from Tauc plots.

280

281 2.5 Solar-driven photocatalytic H₂ evolution

282 Photocatalytic experiments under simulated solar light irradiation were conducted by dispersing
283 0.2 g/L of each photocatalyst in 10 ml of aqueous solution containing 10% (v/v) sacrificial donor
284 (TEOA, MeOH, 5-HMF). The suspension was degassed and saturated with Ar under constant
285 stirring before illumination. Next, the reactor was placed 25 cm away from a 300 W Xe lamp (as
286 described in 2.2.4), which provided solar irradiation at wavelengths $\lambda > 300$ nm for 6 h. At each
287 time interval (1 h), 50 μ l of gas was sampled from the headspace of the gastight reactor and injected
288 into the gas chromatograph (GC). The GC was a Chromatec Crystal 9000 equipped with a TCD
289 detector, operated at 70 °C and 150 °C, oven and detector temperature, respectively. Separation
290 was achieved using a 5 Å molecular sieve column, with N₂ as the carrier gas. Data acquisition and
291 quantification were performed using the Chromatec (Analytic) software, and GC calibration was
292 performed as described in previously published protocols.⁴⁰

293

2.6 Photooxidation of 5-(hydroxymethyl) furfural (5-HMF)

294 The conversion of the platform chemical 5-HMF was investigated as a sacrificial electron donor
295 in aqueous solutions, for H₂ evolution under solar light irradiation, targeting a sustainable process
296 for oxidative production of value-added chemicals such as 2,5-furandicarboxylic acid (FDCA) and
297 2,5-diformylfuran (DFF) coupled with HER. Photocatalytic experiments were conducted using 2-
298 4 mg of catalyst dispersed in 10 ml of either aqueous, MeCN or an 80:20 MeCN: H₂O mixed
299 solvent dispersion, under Ar saturated conditions, unless otherwise stated. The first set of
300 experiments employed 0.2 g/L catalyst concentration, a 10 mM 5-HMF solution in MilliQ H₂O
301 and 12 h of Xe lamp irradiation (as described in 2.2.4). The second set used the same 5-HMF
302 concentration (10 mM) with 0.4 g/L catalyst dosage and shorter irradiation time (6 h) to identify
303 the dominant active species responsible for 5-HMF oxidation. H₂ gas evolved during the reaction
304 was collected from the reactor head space and quantified via GC as in 2.5. Liquid-phase products



305 were analysed by HPLC and UV-Vis after removal of the photocatalyst via filtration and
306 appropriate dilution. HPLC analysis was performed on an Agilent HPLC 1220 Infinity LC System
307 using a C₁₈ reversed-phase column (Poroshell 120 EC-C18, 4 μ m, 4.6 by 150 mm; Agilent). The
308 elution profile (0.75 ml/min) consisted of a 10-min isocratic elution, and the mobile phase was a
309 20% (v/v) MeOH solution. Excitation wavelengths of the detector were set at 230 and 270 nm.
310 The photooxidation of 5-HMF was quantified by UV-Vis spectroscopy (U-2000 (Hitachi,
311 Berkshire, United Kingdom)), monitoring the characteristic absorbance at 284 nm in H₂O and at
312 280 nm in MeCN 80% mixtures. Control experiments with 10 mM 5-HMF in H₂O and MeCN
313 80% for 12 h and 6 h light duration experiments without catalyst and under Ar atmosphere, were
314 conducted for comparison and revealed negligible photolysis of 5-HMF. The samples used for
315 HPLC and UV-Vis spectroscopy were diluted to 50 μ M and 200 μ M respectively, based on the
316 concentration of 5-HMF before light irradiation.

317

318 3. Results and Discussion

319 3.1 Structural and morphological characterization

320 The successful synthesis of copper-substituted Freudenbergite (Cu-FDT) was confirmed
321 through Rietveld refinement of powder X-ray diffraction (PXRD) data. The experimental pattern
322 of the synthesized material matched the reference pattern for stoichiometric Freudenbergite
323 (FeNaTi₃O₈, COD No. 9011187), which crystallizes in the monoclinic C12/m1 space group.
324 Refinement indicates that Cu²⁺ ions substitute for Fe³⁺ within the Freudenbergite tunnel structure
325 (**Figure 1a, Figure S1, Table S1**). Charge balance is likely maintained by the coexistence of Ti³⁺
326 and Ti⁴⁺. The most intense diffractions were observed at $2\theta = 10.1^\circ, 11.1^\circ, 23.8^\circ, 24.4^\circ, 28.7^\circ$,



327 29.7° , 44.3° , 47.7° , and 67.1° and were indexed to the (001), (200), (110), (002), (111), (310),
 328 (003), (020), and (023) lattice planes, respectively. A minor, unidentified impurity phase (<1 wt%)
 329 was detected but considered negligible for the structural analysis. Notably, the addition of a Cu^{2+}

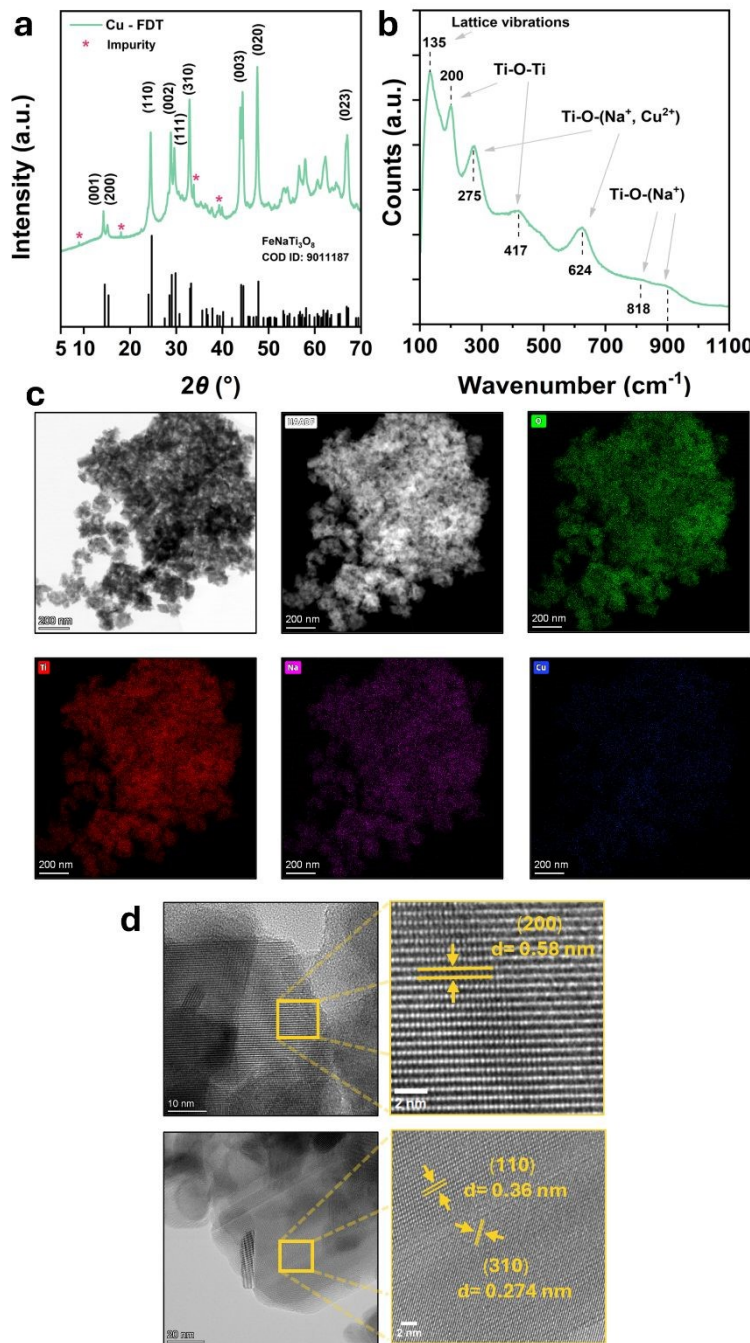


Figure 1. **a)** PXRD pattern of Cu-FDT and of Freudenbergite presented for reference, **b)** Raman spectra of the synthesized material, **c)** STEM and elemental maps of O, Ti, Na and Cu, **d)** HR-TEM images and d-spacing of the selected areas.

330 precursor was essential for the crystallization of the Freudenbergite phase. Reaction mixtures
331 without the Cu²⁺ precursor resulted exclusively in the crystallization of anatase TiO₂, which was
332 used for comparison. The Cu-FDT material was found to exhibit an average crystallite size of 22.4
333 \pm 0.2 nm measured on the (020) direction (**Table S3**). Data quality made the calculation of
334 microstrain due to substitution of Fe³⁺ with Cu²⁺ and the contribution from the existence of oxygen
335 defects near Ti³⁺ positions not possible. Nonetheless, differences in the intensity of certain
336 diffractions between calculated and the experimental pattern indicate subtle changes in bond length
337 due to Cu²⁺ incorporation (**Figure S1**). More specifically, the refined lattice parameters were
338 determined to be $a = 1.2245(1)$ nm, $b = 0.38209(4)$ nm, $c = 0.64920(8)$ nm and $\beta = 107.68^\circ$ (**Table**
339 **S1**). A comparative analysis with the pristine lattice parameters of the referenced .cif file reveals
340 a discernible shift from the pristine Fe³⁺ bearing Freudenbergite (FeNaTi₃O₈). The observed
341 anisotropic changes in the unit cell and especially the contraction of the a and b parameters, $\Delta a = -$
342 0.0022 nm and $\Delta b = -0.0002$ nm respectively, as well as the expansion along the c axis and the
343 significant increase in the β angle, $\Delta c = 0.0009$ and $\Delta \beta = 0.52^\circ$, are attributed to the successful
344 incorporation of Cu²⁺ in the crystal structure.²⁵ This distorted pattern is characteristic of the Jahn-
345 Teller effect, a well-known phenomenon of d⁹ cations like Cu²⁺. This effect causes a cooperative
346 elongation of the (Cu/Ti)O₆ octahedra, while the substitution of Fe³⁺ (0.065 nm) by the larger Cu²⁺
347 (0.073 nm) ion is the primary reason for the observed structural changes. Regarding charge
348 neutrality of the crystal lattice, the incorporation of divalent copper in a structure typically
349 balanced by trivalent cations indicates a charge compensation mechanism. The observed
350 expansion along the c axis is consistent with the co-existence of a larger cation in the octahedral
351 sites. This suggests that a portion of Ti⁴⁺ (0.605 nm) is reduced to Ti³⁺ (0.67 nm) to maintain
352 neutrality in the new crystal lattice. The combined effects of the Jahn-Teller effect induced by Cu²⁺
353 and the possible presence of Ti³⁺ could explain the calculated differences in the crystal lattice of
354 Cu-FDT in comparison to the known structure of Freudenbergite.^{41,42}

355 Raman spectroscopy provided further understanding into the bonding environment of the
356 Cu-FDT unit cell (**Figure 1b**). The framework of the Freudenbergite, being structurally analogous
357 to titanate nanotubes, contains edge- and corner- sharing TiO₆ octahedra. This similarity results in
358 vibrational spectra varying significantly from the more densely packed frameworks of well-known
359 TiO₂ polymorphs like anatase and rutile. Here, the spectrum is defined by bands at 135 cm⁻¹,
360 associated with lattice vibrations at 200 and 417 cm⁻¹ assigned to Ti-O-Ti bending and stretching
361 vibrations.⁴³ The features at 275 and 624 cm⁻¹ are associated with metal-oxygen bonds (Ti-O-Na⁺
362 or Cu²⁺).⁴⁴ Furthermore, the higher-frequency bands at 818 and 900 cm⁻¹ are indicative of Ti-O-
363 Na stretching modes. The red-shifting of the band at 624 cm⁻¹ as compared to Fe³⁺-containing
364 Freudenbergite implies the existence of Cu²⁺ and is directly correlated to bond elongation due to
365 the Jahn-Teller effect induced by the latter.^{43,44}

366 Elemental mapping via STEM-EDS confirmed the homogenous distribution of oxygen
367 (O), titanium (Ti), sodium (Na) and copper (Cu) throughout the surface of the new material,
368 indicating a uniform elemental composition (**Figure 1c**). Quantitative analysis of the EDS spectra
369 yielded an overall elemental stoichiometry distinct from CuNaTi₃O₈, primarily due to significantly
370 higher sodium content (**Table S2**). Excess sodium can be explained by residual Na⁺ ions on the
371 surface of the material contributing to the amorphous part of the sample rather than the unit cell of
372 Cu-FDT.

373 HR-TEM images of the synthesized photocatalyst confirmed interplanar crystal spacings
 374 of 0.58 nm, 0.36 nm and 0.274 nm assigned to (200), (110) and (310) facets of the Freudenbergite
 375 unit cell respectively (**Figure 2d**, **Figure S2c**). The synthesized material exhibited predominantly
 376 a nanoplatelet-like morphology and heavy aggregation, a phenomenon arising from the co-
 377 precipitation and dehydration steps comprising the synthetic procedure. Image analysis revealed a
 378 polydisperse size distribution with an average size at 23.3 nm with most of the particles measuring
 379 less than 50 nm (**Figure S2a, b**).

380 The XPS survey spectra for Cu-FDT confirmed the presence and oxidation states of Ti,
 381 Cu, O and Na which comprise the unit cell of Cu-FDT (**Figure S3a**). Determination of Ti valences
 382 present is pivotal for understanding the mechanism behind the charge balancing in the unit-cell of
 383 the synthesized material. The replacement of Fe^{3+} with Cu^{2+} necessitates such a mechanism
 384 through the partial reduction of Ti^{4+} to Ti^{3+} and possibly the co-existence of O vacancies near the
 385 Ti^{3+} ions. High resolution analysis of the Ti 2p core level revealed a doublet with spin-orbit
 386 splitting of 5.75 eV. The spectrum was characterized by a primary doublet with the $\text{Ti} 2p_{3/2}$ peak
 387 at 459 ± 0.1 eV, assigned to Ti^{4+} in the TiO_6 octahedra of a TiO_2 -like environment. Critically, a
 388 second doublet was identified at a lower binding energy ($\text{Ti} 2p_{3/2}$ at 458 ± 0.1 eV), which was
 389 attributed to the presence of Ti^{3+} species.⁴⁵ Ti^{3+} contribution was calculated to be 12.5% for the
 390 total amount of Ti present in the sample (**Table S3**). The Cu 2p_{3/2} spectra main feature, located at
 391 933.5 eV indicated the presence of copper in the 2⁺ state (**Figure 2b**) while the Na 1s spectrum at

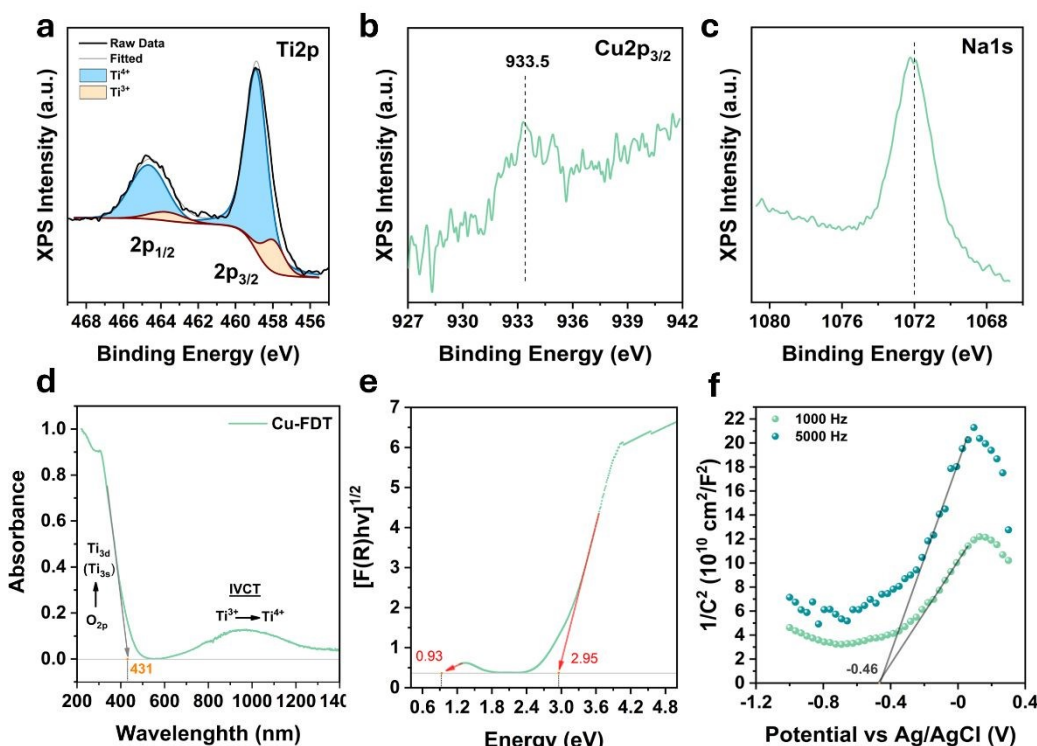


Figure 2. **a-c)** Fitted XPS spectra of the Ti 2p core level (**a**), Cu 2p_{3/2} core level (**b**), and Na 1s core level (**c**), **d)** UV-DRS absorbance spectra of Cu-FDT photocatalyst, **e)** Tauc plot constructed from the Kubelka-Munk transformation of Cu-FDT reflectance spectra, **f)** Mott-Schottky plots obtained at 1000 and 5000 Hz.

1072 eV was consistent with Na-Ti-O bonding (**Figure 2c**).⁴⁶⁻⁴⁸ The C 1s peak was deconvoluted into three components corresponding to C-C/C-H, C-O, and O-C=O bonds (**Figure S3b**) indicating the presence of residual acetates on the surface of Cu-FDT as a consequence of the use of acetic acid and acetone during synthesis.⁴⁹

396

397 3.2 Optical and electrochemical characterization

Optical characterization via UV-DRS provided critical insights into the electronic properties and band structure of the synthesized Cu-FDT material. The Tauc plot derived from the transformed reflectance spectrum revealed an indirect E_g value of 2.95 eV (**Figure 2e**), corresponding to an absorption edge at 431 nm (**Figure 2d**). The bandgap transition, based on the unit-cell configuration, involved the excitation of an electron from the O 2p orbital-consisting valence band (VB) to the conduction band (CB) comprised of hybridized states from $\text{Ti}^{3+}/\text{Ti}^{4+}$ and Cu^{2+} . Furthermore, a distinct low-energy absorption band was observed at approximately 965 nm (0.93 eV) (**Figure 2d, e**). This band lied at considerably longer wavelengths than typical Cu^{2+} d-d transitions that could potentially be immobilized on the semiconductor's surface and exhibited characteristics consistent with an intervalence charge transfer (IVCT) process.⁵⁰ The broad, asymmetric shape and energy of this transition suggests electron transfer between adjacent mixed-valence sites, most likely between Ti^{3+} and Ti^{4+} centres or from Cu^{2+} to Ti^{4+} . This IVCT band provided strong evidence of electronic coupling between metal centres in the mixed-valence Cu-FDT crystal system, further confirming the successful integration of Cu into the titanate framework and the creation of new electronic states within the bandgap.^{50,51}

To elucidate the electronic band structure and thermodynamic potentials of the Cu-FDT photocatalyst, electrochemical characterization was conducted. Mott-Schottky plots were constructed and the negative slope obtained revealed that Cu-FDT is a n-type semiconductor.⁵² As a result the flat-band potential was used to approximate the conduction band edge position, as for n-type semiconductors the flat-band potential is known to lie close to the CB (**Figure 2f**).⁵³ The energy of the CB minimum defined the thermodynamic driving force of the photoexcited electrons to participate in reduction reactions, such as HER. Two different frequencies (100 and 5000 Hz) were used to ensure reproducibility, and the flat-band potential was calculated to be -0.46V vs Ag/AgCl. Conversion to NHE (pH=7) was performed using formula (2) and the CB of Cu-FDT was determined to be at -0.25 V vs NHE using equation (2).⁵⁴ By correlating the bandgap energy value obtained from the Tauc plot with the experimentally determined conduction band potential, the valence band maximum of Cu-FDT was identified as +2.7 V vs NHE employing relation (3). This electronic structure positions Cu-FDT as a highly promising material for both photocatalytic oxidation processes and HER, as it provides strong oxidative VB and sufficiently reductive CB.⁴

428

429 3.3 Fabrication of Cu-FDT/TiO₂ heterojunctions and surface Na⁺ effect on the 430 heterojunction formation



431 The intentional *in situ* construction of a heterojunction between copper substituted
 432 Freudenbergite (Cu-FDT) and TiO_2 polymorphs was pursued in order to create an efficient
 433 heterojunction for sufficient charge separation and increased HER activity under solar light.
 434 Interestingly, the addition of a minimal amount of water (0.5% v/v) during synthesis induced the
 435 co-crystallization of anatase TiO_2 along with Cu-FDT, which constituted 34.5% of the crystalline
 436 phase in the final composite and at the same calcination temperature and duration (**Figure 3a**,
 437 **Figure S4a**, **Table S4**). A series of calcination experiments revealed the thermal evolution of the
 438 multiphase system, consisting of anatase, rutile, or both, alongside Cu-FDT. When the synthesis
 439 reaction product was subjected to calcination at $650^\circ\text{C}/4\text{h}$, a portion of the metastable anatase
 440 transformed into rutile, resulting in a three-phase system (Cu-FDT, anatase and rutile) with Cu-
 441 FDT remaining the main crystalline constituent at 47.2%. Further increase of the calcination
 442 temperature at 750°C , produced a dual-phase system consisting of Cu-FDT and rutile in a 1:1 ratio,
 443 as a result of the complete transformation of anatase to rutile.⁵⁵ Interestingly, higher calcination
 444 temperatures (850°C) induced a profound phase transformation: the Cu-FDT content drastically
 445 diminished, concurrent with the crystallization of a copper and sodium titanate perovskite-type
 446 phase, identified as $\text{Na}(\text{Cu}_{2.5}\text{Ti}_{0.5})\text{Ti}_4\text{O}_{12}$ cubic perovskite.⁵⁶ This observation suggests that higher
 447 calcination temperatures induced a solid-state transition between the Freudenbergite and
 448 perovskite structures. The crystalline size of the main constituents was calculated through Rietveld
 449 Refinement of the powder diffraction pattern for each photocatalyst, with the exemption of Cu-
 450 FDT_A sample for which anatase crystallite size could not be safely calculated due to peak overlap
 451 with Cu-FDT. The crystallite size of the Cu-FDT phase exhibited a clear upward trend with

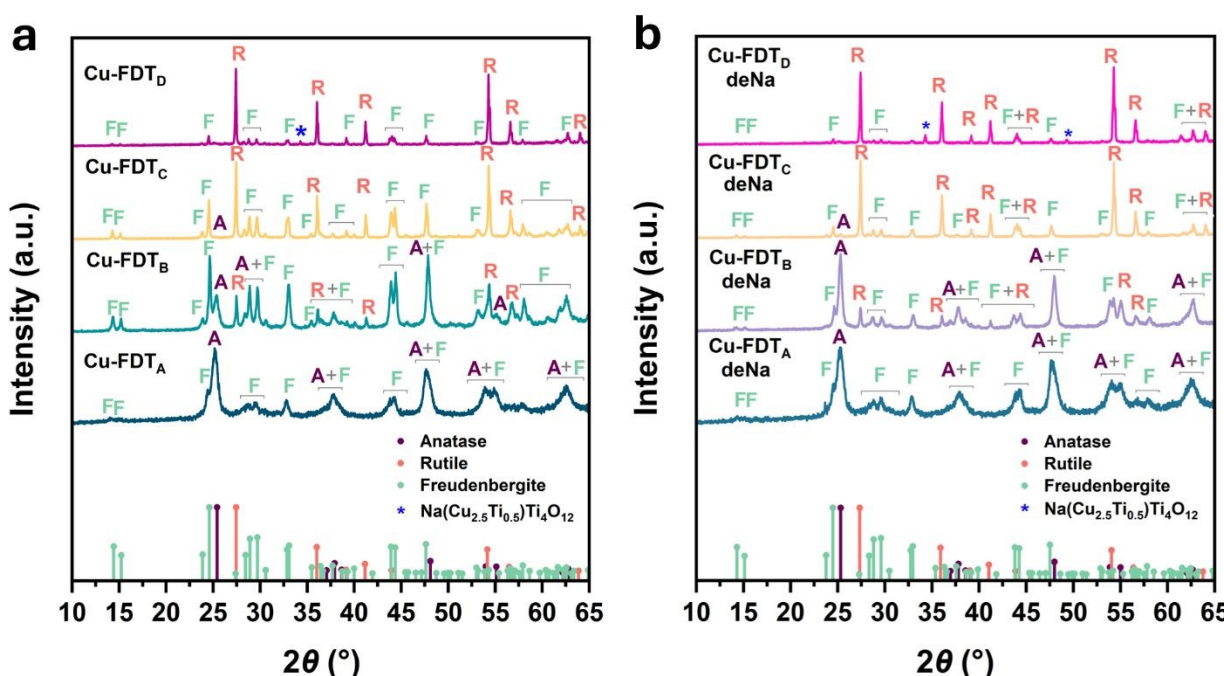


Figure 3. Effect of calcination temperature on crystalline phase composition of samples **a)** Cu-FDT_{A-D} with excess Na^+ and **b)** Cu-FDT_{A-D} deNa with stoichiometric Na^+ . A: Anatase, R: Rutile, F: Freudenbergite.

452 increasing calcination temperature, increasing from 22.4 nm for the sample containing only
453 anatase and Cu-FDT (Cu-FDT_A) to a maximum of 106.5 nm in the sample calcined at the highest
454 temperature (**Figure S4, Table S4**). This growth can be attributed to Ostwald ripening, a thermally
455 driven process where larger particles grow at the expense of smaller, less stable ones.⁵⁷ Notably,
456 the co-crystallization with anatase in the initial Cu-FDT_A sample appeared to suppress the growth
457 of Cu-FDT crystallites, constraining them to a size of 10.3 nm. Concurrently, the rutile phase first
458 emerged in the sample Cu-FDT_B with a crystalline size of 73.11 nm. The rutile crystallites also
459 underwent significant growth through Ostwald ripening, ultimately reaching 131.4 nm in sample
460 Cu-FDT_D.

461 To mitigate the detrimental impact of excess sodium surface Na⁺ species, which can act as
462 charge recombination centres and suppress photocatalytic activity, a second set of catalysts was
463 prepared following the same calcination protocol, but the starting product of the reaction was
464 subjected to 1 M HCl treatment under ultrasonication to remove surface sodium.⁵⁸ This established
465 purification process effectively eliminates alkali-containing impurities, exposing catalytically
466 active sites and potentially enhancing the HER activity of the photocatalysts. After excess sodium
467 removal from the reaction product, the desodiated (deNa) series of photocatalysts followed a
468 similar crystallization pathway to their sodium-rich counterparts, with anatase, rutile and NaCuTi-
469 perovskite nucleating at the same calcination temperatures (**Figure 3, Table S4**). However, the
470 thermal stability of anatase was notably altered. Specifically, it demonstrated significantly
471 enhanced resilience to thermal transformation in the deNa samples, contributing to 39.4% of the
472 crystalline phase in the Cu-FDT_B deNa sample, compared to only 22.5% in the sodium-rich Cu-
473 FDT_B sample calcined at the same temperature. A minor anatase fraction (1.5%) persisted even
474 after calcination at 750°C (Cu-FDT_C). Furthermore, the crystallite size of the Cu-FDT phase, while
475 still following an upward trend with temperature, was consistently smaller across all deNa samples
476 after 1 M HCl treatment (**Figure S4, Table S4**). Finally, the perovskite phase that formed at 850°C
477 was present in substantially larger proportion (10.2% vs. 3.9%) following sodium removal. This
478 suggests that the elimination of excess surface sodium had a direct impact on the crystallization
479 process and the heterojunctions formed, while it enhanced this specific solid-state transition
480 (**Figure 3, Table S4**).
481

482 3.4 Solar-driven photocatalytic H₂ evolution

483 The photocatalytic hydrogen evolution activities of the synthesized photocatalysts,
484 including bare Cu-FDT, were evaluated under simulated solar light irradiation using TEOA as the
485 sacrificial electron donor. As shown in **Figure 4a** and **4e**, bare Cu-FDT exhibited modest HER
486 activity, with an average hydrogen evolution rate of 31.9 $\mu\text{molH}_2\cdot\text{g}^{-1}\cdot\text{h}^{-1}$. The low activity is likely
487 attributable to rapid charge-carrier recombination, a common issue in semiconductor
488 photocatalysts lacking a co-catalyst, as well as to the weak reducing character of the Cu-FDT CB
489 position.⁵⁹

490 In contrast, the Cu-FDT_A sample, which contains a heterojunction between Cu-FDT and
491 anatase, demonstrated a drastically enhanced hydrogen evolution rate at 702.7 $\mu\text{molH}_2\cdot\text{g}^{-1}\cdot\text{h}^{-1}$
492 (**Figure 4b, e**). This twenty-two-fold enhancement in the catalytic activity can be attributed to the
493 *in situ* formation of an efficient heterojunction that significantly improves charge separation. The
494 intimate interfacial contact achieved through the concurrent growth and crystallization of Cu-FDT

495 and anatase phases facilitates the creation of an internal electric field, potentially via a Type-II or
496 Z-scheme charge transfer mechanism, thereby suppressing recombination and enhancing

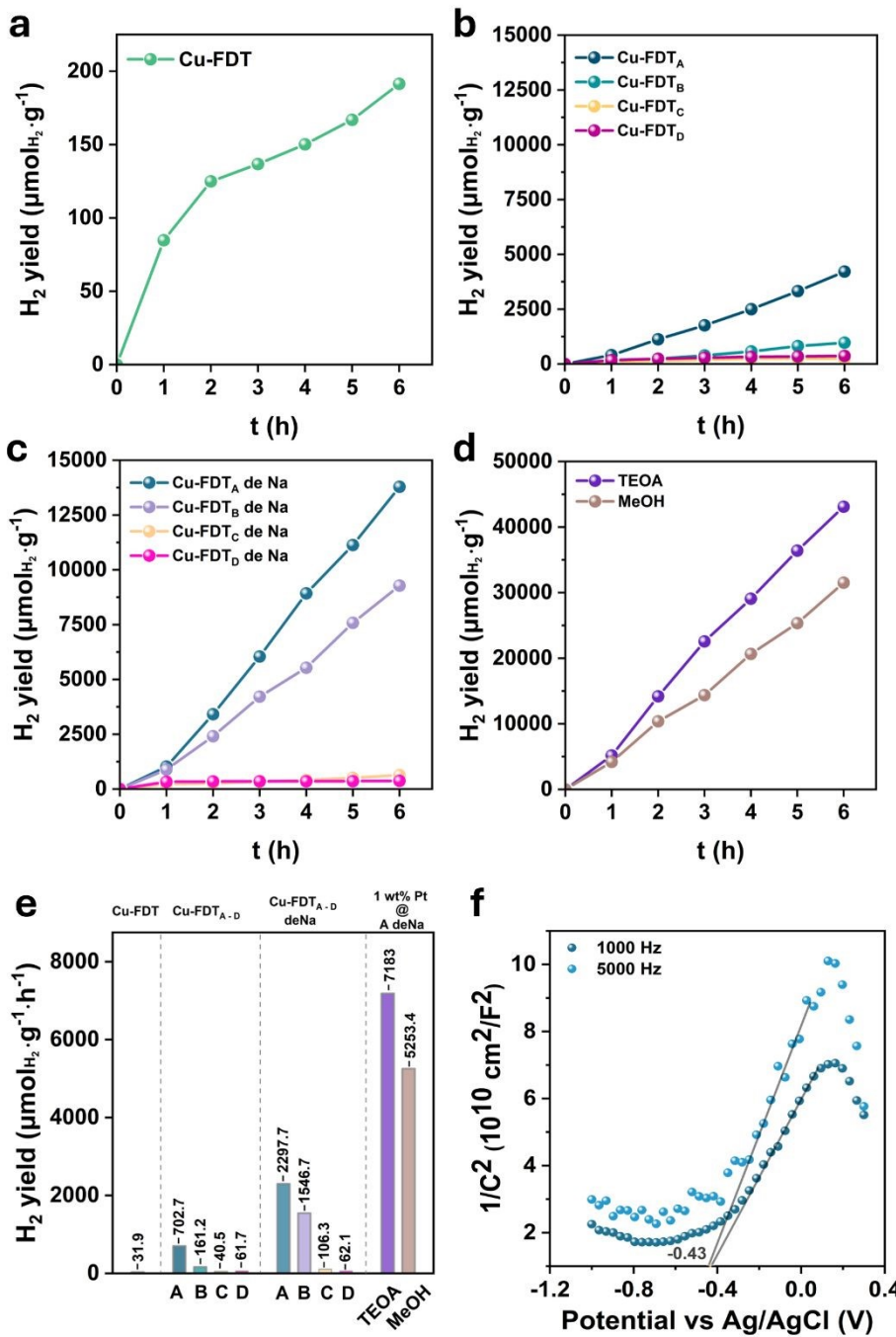


Figure 4. H₂ evolution over the course of 6 h employing **a)** bare Cu-FDT, **b)** the sodium-rich heterojunctions in samples Cu-FDT_{A-D}, **c)** the desodiated heterojunctions in samples Cu-FDT_{A-D} deNa, **d)** TEOA and MeOH as sacrificial donors for the 1 wt% Pt photodeposited Cu-FDT_A deNa photocatalyst*. **e)** Average H₂ evolution rates for all systems tested* **f)** Mott-Schottky plots for the Cu-FDT_A deNa sample.

*Results for 1 wt% Pt @ Cu-FDT_A omitted for clarity.

497 photocatalytic efficiency. However, HER performance declined to $161.2 \mu\text{mol}_{\text{H}_2} \cdot \text{g}^{-1} \cdot \text{h}^{-1}$ in the
 498 three-phase system (Cu-FDT, anatase and rutile) in sample Cu-FDT_B (**Figure 4b, e**). The rate
 499 reduction is likely due to the unfavorable electronic band structure of rutile, which may act as a
 500 charge recombination center, combined with the decreased anatase content resulting from its phase
 501 transition to rutile.

502 Finally, samples calcined at higher temperatures (Cu-FDT_C and Cu-FDT_D) exhibited only
 503 trace amounts of H_2 . This complete loss of activity can be attributed to the absence of the effective
 504 Cu-FDT/anatase heterojunction and the significant increase in nanoparticle size across all
 505 remaining phases, a consequence of excessive sintering, which reduces the available surface area
 506 and impedes charge transfer to the photocatalyst surface (**Figure 4b, e**). It should be noted that the
 507 hydrogen evolution vs. time plots for all catalytically active samples exhibited a linear trend over
 508 the 6-hour irradiation period. This linearity indicates stable photocatalytic activity and suggests no
 509 significant photo corrosion or deformation of the catalyst surfaces under the employed reaction
 510 conditions.

511 A dramatic enhancement in photocatalytic hydrogen evolution activity was observed for
 512 the deNa catalyst series (**Figure 4c, e**). The overall performance trend among the different phases
 513 remained consistent with that of the sodium-rich analogues: samples Cu-FDT_C deNa and Cu-FDT_D
 514 deNa exhibited minimal activity. However, a remarkable enhancement was recorded for the Cu-
 515 FDT/anatase heterojunction in sample Cu-FDT_A deNa, which achieved an average hydrogen
 516 evolution of $2297.7 \mu\text{mol}_{\text{H}_2} \cdot \text{g}^{-1} \cdot \text{h}^{-1}$. This corresponds to more than three-fold increase compared to
 517 its sodium-rich counterpart and reveals the true potential of this heterojunction when all catalytic
 518 active surface sites are accessible. The mixed-phase sample, Cu-FDT_B deNa, exhibited the second
 519 highest activity at $1546.7 \mu\text{mol}_{\text{H}_2} \cdot \text{g}^{-1} \cdot \text{h}^{-1}$. Although significant, this performance remains limited
 520 by the presence of rutile, which, as previously noted, acts as a charge recombination center and
 521 thus bottlenecks the overall catalytic efficiency. The pronounced activity increase across the deNa
 522 series demonstrates that the removal of excess Na is a pivotal post-synthetic treatment for this
 523 system as it eliminates insulating species from the photocatalytic surfaces.

524 Photoluminescence (PL) spectroscopy recorded under 310 nm excitation was employed to
 525 provide insight into the charge carrier dynamics of the individual components and the co-
 526 crystallized and desodiated Cu-FDT/anatase (Cu-FDT_A deNa) heterojunction. The pristine TiO_2
 527 sample exhibited the strongest PL emission, while Cu-FDT showed a comparatively lower
 528 intensity. Notably, the Cu-FDT_A deNa composite displayed significant quenching of PL compared
 529 to its bare constituents. This substantial reduction in emission intensity suggests that co-
 530 crystallization promotes intimate interfacial contact and facilitates efficient charge separation
 531 across the heterojunction, thereby suppressing radiative recombination pathways.⁶⁰

532 The better performing photocatalysts of both series containing the Cu-FDT/anatase
 533 heterojunction, namely CuFDT_A and Cu-FDT_A deNa, were selected for further investigation and
 534 catalytic optimization. To this end, 1 wt% Pt was photodeposited onto each sample to function as
 535 a co-catalyst. Pt is widely regarded as the benchmark co-catalyst for HER due to its optimal Fermi
 536 level alignment with the CB of many semiconductors, such as anatase- TiO_2 , which promotes
 537 efficient electron extraction and accumulation, coupled with its exceptionally low overpotential
 538 for proton reduction.⁴ The deposition of 1 wt% Pt as a co-catalyst yielded strikingly divergent
 539 outcomes for the two catalysts. The desodiated sample, Cu-FDT_A deNa, exhibited a remarkable



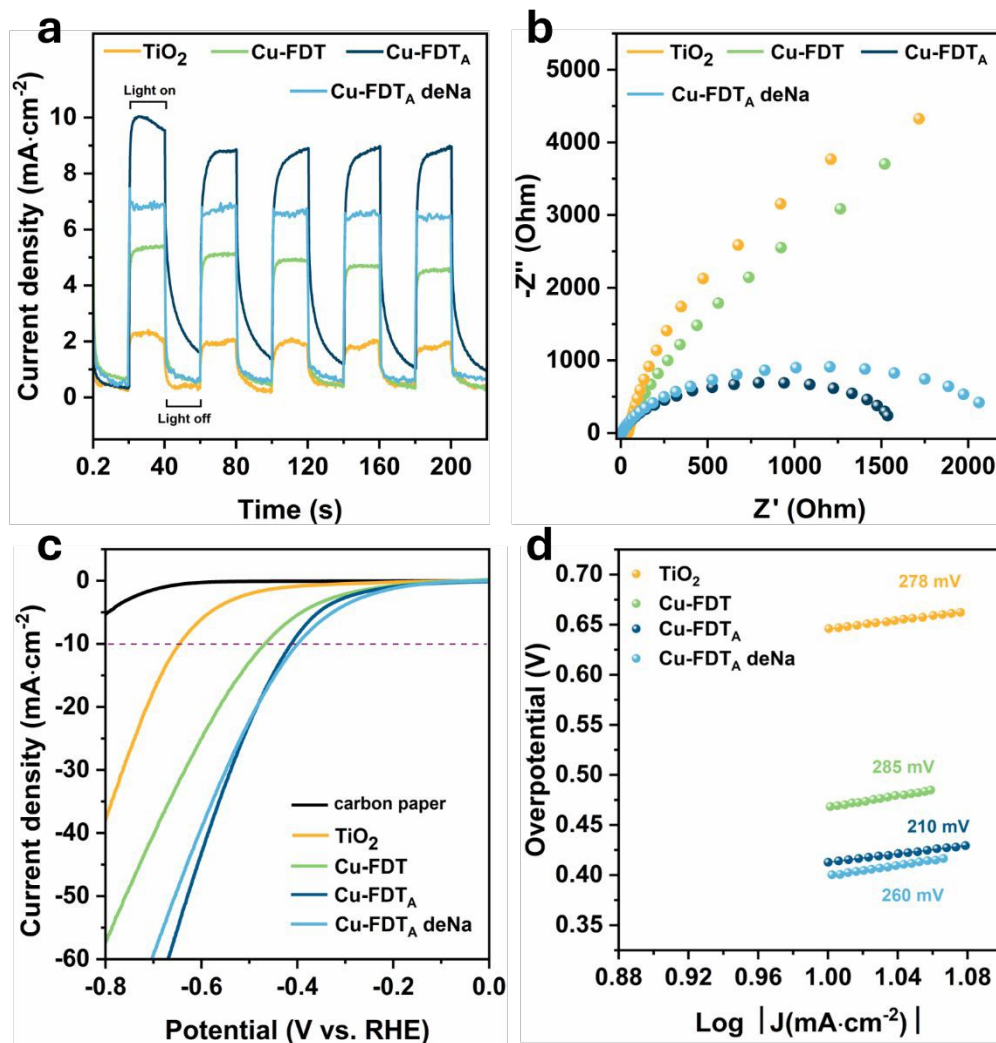


Figure 5. **a)** Photocurrent density response of the synthesized photocatalysts under bias of 0.5 V vs. Ag/AgCl, **b)** EIS Nyquist plots of the synthesized photocatalysts at 0 V vs. Ag/AgCl, **c)** LSV HER polarization curves of carbon paper (electrode substrate) and the synthesized photocatalysts recorded in 0.5 M H₂SO₄, **d)** Corresponding Tafel slopes for HER.

540 enhancement in photocatalytic performance, achieving an average hydrogen evolution rate of 7183
 541 $\mu\text{mol}_{\text{H}_2} \cdot \text{g}^{-1} \cdot \text{h}^{-1}$ in the presence of triethanolamine (TEOA) as a sacrificial electron donor, while
 542 upon substitution of TEOA with MeOH the performance dropped to 5253.4 $\mu\text{mol}_{\text{H}_2} \cdot \text{g}^{-1} \cdot \text{h}^{-1}$ (**Figure 4d**). This implies that the catalyst works better under alkaline pH (reaction pH= 11) compared to
 543 the use of acidic MeOH as a sacrificial electron donor. The superior activity observed with TEOA
 544 indicated that the catalyst operates more efficiently via the H₂O reduction pathway than the proton
 545 (H⁺) reduction one. The alkaline environment supplied by 10% TEOA, facilitated the activation
 546 and reduction of water molecules at the catalyst surface. The significantly lower performance in
 547 the acidic conditions created by 10% MeOH suggests the limited presence of catalytic sites that
 548 favor H⁺ adsorption and reduction (**Figure 4d, e**). Conversely, Pt deposition to the sodium-rich
 549



550 Cu-FDT_A photocatalyst had an adverse effect, resulting in complete deactivation of the
551 photocatalyst. We propose that in the sodium-rich sample, excess surface Na⁺ formed an insulating
552 layer that inhibited the formation of an effective Pt-heterojunction Schottky junction. Instead, the
553 deposited Pt nanoparticles likely functioned as efficient recombination centers for photogenerated
554 charges, thereby quenching all photocatalytic activity. In the desodiated sample, the removal of
555 this passivating layer allowed for optimal interfacial contact between Pt and the semiconductors,
556 facilitating efficient extraction of electrons (e⁻) via the Schottky junction and their subsequent use
557 for H₂O reduction.⁶¹

558

559 **3.5 Photoelectrochemical performance of the Cu-FDT_A and Cu-FDT_A deNa heterojunctions**

560 The interfacial charge transfer dynamics and electrocatalytic activity of the Cu-
561 FDT/anatase heterojunction, in both its as-synthesized (Na⁺-rich) and HCl-washed (desodiated)
562 forms, were investigated through transient photocurrent response, EIS and LSV measurements.
563 The transient photocurrent and EIS measurements, conducted in a neutral Na₂SO₄ electrolyte
564 probed the bulk and interfacial charge separation efficiency of the heterojunctions and the
565 individual heterojunction components TiO₂ anatase and Cu-FDT. The Na⁺-rich heterojunction
566 (Cu-FDT_A) exhibited a stronger instantaneous photocurrent response to solar light (**Figure 5a**)
567 than the desodiated counterpart (Cu-FDT_A deNa) while Cu-FDT generated more current than
568 anatase TiO₂ upon simulated solar-light irradiation. Since the only difference between the two
569 photocatalysts is the existence or lack thereof of surface Na⁺ the difference in photogenerated
570 charge carrier is assigned to a Na⁺-induced modification of the heterojunction-electrolyte
571 interfacial environment. It has been shown that electrolyte cations, including Na⁺, can act as
572 positive surface dipoles, inducing a downward band bending that creates a stronger electric field
573 and drives enhanced charge separation.⁶² Such interfacial electrostatic effects rationalize the
574 superior transient photocurrent observed for the Cu-FDT_A heterojunction, where excess Na⁺ is
575 strongly adsorbed on the metal-oxide surface, while the reduced photocurrent following
576 desodiation is consistent with partial attenuation of this favorable interfacial field, despite retention
577 of heterojunction-enabled charge separation.

578 EIS plots further support this conclusion, as Cu-FDT_A exhibits a marginally smaller
579 semicircle radius in the Nyquist plot compared to the optimal for photocatalytic HER, Cu-FDT_A
580 deNa, indicating a lower effective interfacial charge-transfer resistance (**Figure 5b**). Both
581 heterojunctions revealed greatly reduced charge-transfer resistance than the bare components Cu-
582 FDT and TiO₂ anatase which indicates the creation of an effective heterojunction.

583 To further probe the effectiveness of the created heterojunction for HER, LSV was performed in
584 0.5 M H₂SO₄. Pristine TiO₂ anatase required the highest overpotential to drive HER, followed by
585 Cu-FDT. In contrast, both Cu-FDT_A and Cu-FDT_A deNa heterojunctions exhibited significantly
586 lower overpotentials and similar polarization behavior. Notably the desodiated catalyst (Cu-FDT_A
587 deNa) initiated the HER at a slightly more positive onset potential (**Figure 5c**). This trend suggests
588 that the beneficial role of Na⁺ observed under illumination does not directly translate into improved
589 electrocatalytic HER activity in acidic media. We attribute this to surface-associated Na⁺ ions
590 partially block H⁺-accessible sites, thereby hindering proton adsorption and hydrogen evolution
591 relative to the freely accessible surface of the desodiated catalyst Cu-FDT_A deNa.



592 Tafel analysis, derived from the LSV data, provides complementary insights into the
 593 reaction kinetics. Pristine TiO_2 anatase and Cu-FDT exhibit Tafel slopes at 278 and 285 $\text{mV}\cdot\text{dec}^{-1}$,
 594 respectively. The formation of the Cu-FDT/anatase heterojunction substantially improved the
 595 kinetics, reducing the Tafel slopes to 210 $\text{mV}\cdot\text{dec}^{-1}$ for Cu-FDT_A and 260 $\text{mV}\cdot\text{dec}^{-1}$ for Cu-FDT_A
 596 deNa (**Figure 5d**). The superior onset potential of the desodiated sample, despite its higher Tafel
 597 slope, indicates that desodiation creates a surface that HER commences more readily, likely due
 598 to improved accessibility of active sites and enhanced electronic coupling with the Pt co-catalyst
 599 used for photocatalytic HER.

600 To elucidate the charge transfer mechanism within the Cu-FDT_A deNa heterojunction,
 601 electrochemical impedance measurements were conducted to differentiate between a conventional
 602 Type-II and a direct Z-scheme pathway. The band edge positions of the anatase reference prepared
 603 under identical conditions but in the absence of Cu^{2+} , were derived from the Mott-Schottky Figure
 604 5) -0.79 V vs Ag/AgCl, corresponding to a CB minimum at -0.6 V vs NHE. Based on a bandgap
 605 of 3.21 eV, its VB maximum was calculated to reside at +2.61 V vs NHE (**Figure S6 and S7**),
 606 consistent with literature values for anatase TiO_2 .⁶³ In contrast, the Cu-FDT_A deNa heterojunction

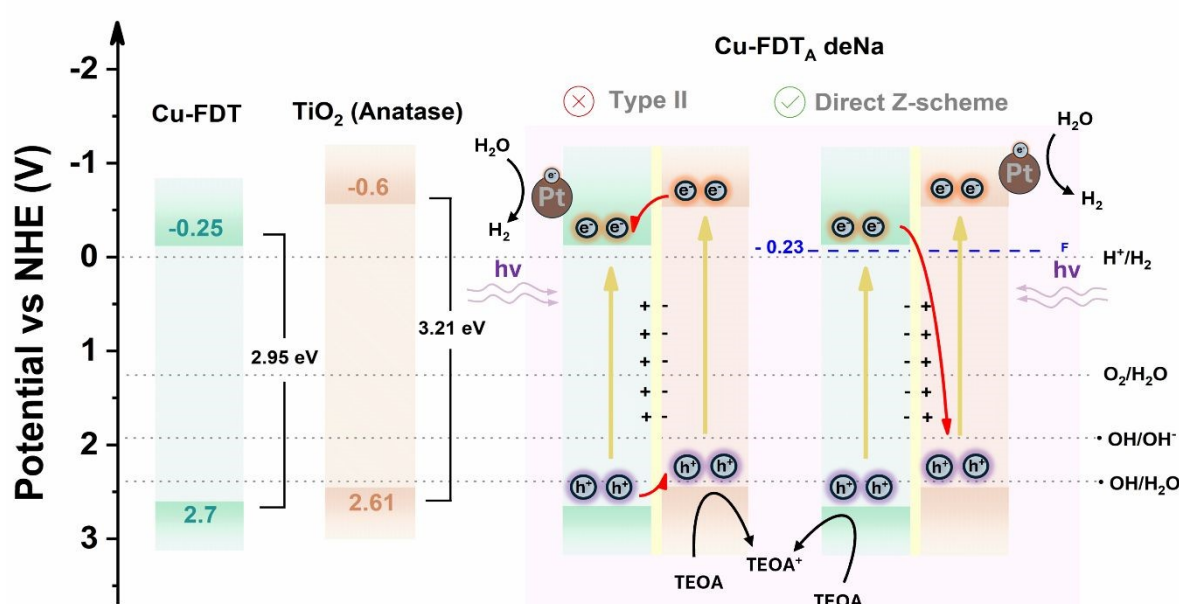


Figure 6. Proposed Z-scheme charge-transfer for HER and oxidation of TEOA employing the 1 wt% Pt @ Cu-FDT_A deNa photocatalyst.

607 exhibited a composite flat-band potential that was shifted anodically to -0.43 V vs. Ag/AgCl. This
 608 positive displacement of the apparent flat-band potential relative to the conduction bands of the
 609 constituent semiconductors suggests the formation of an internal electric field across the interface
 610 and indicated a modified interfacial electronic structure.⁶⁴ Such anodic shift can be interpreted as
 611 supporting a direct Z-scheme configuration, in which selective charge recombination occurs
 612 between e^- in the CB of Cu-FDT and the h^+ in the VB of anatase, rather than the delocalized charge

613 redistribution typical of a Type-II junction (**Figure 6**).⁶⁵ In this configuration, photoexcitation of
614 both semiconductors with solar-light promotes charge carrier separation, preserving the most
615 energetic species, that are the h^+ in the highly oxidative VB of Cu-FDT and the e^- in the CB of
616 anatase. These remaining carriers subsequently participate in surface redox reactions, where the
617 h^+ oxidize TEOA and the e^- are transferred to the Pt co-catalyst to promote HER. Although we
618 cannot completely rule out the existence of a Type II heterojunction between these materials, the
619 observed anodic shift, when considered together with the relative band edge positions and the
620 known electronic structure of both phases, provides compelling electrochemical evidence
621 consistent with a direct Z-scheme mechanism rather than a conventional Type-II heterojunction.
622 (**Figure 6**).^{66,67}

623

624 3.6 Solar driven photooxidation of 5-(hydroxymethyl)furfural (5-HMF)

625

626 To evaluate the potential for a concurrent dual-function process coupling H_2 evolution
627 with 5-HMF oxidation, initial experiments were carried out using the top performing HER
628 photocatalysts, Cu-FDT_A and Cu-FDT_A deNa along with their Pt loaded counterparts, with 5-HMF
629 serving as the sole electron donor (**Figure S8**). The results confirmed that 5-HMF can effectively
630 act as an electron donor for these systems. The maximum H_2 evolution rate reached 297.4
631 $\mu\text{mol}_{H_2} \cdot \text{g}^{-1} \cdot \text{h}^{-1}$ for 1 wt% Pt @ Cu-FDT_A. Notably, while Pt photodeposition enhanced the HER
632 activity of the sodium-rich photocatalyst (Cu-FDT_A), its performance was comparable to the
633 unloaded desodiated catalyst (Cu-FDT_A deNa). Interestingly, Pt loading on Cu-FDT_A deNa
634 resulted in complete catalyst deactivation. This suggests that Na removal significantly alters the
635 catalyst surface, leading to a stronger Pt-support interaction that blocks active sites required for 5-
636 HMF adsorption and oxidation, thereby suppressing the coupled redox process.^{68,69}

637 To evaluate the oxidation performance and selectivity of the synthesized Cu-FDT/anatase
638 heterojunctions which showed the highest activity for solar driven HER as well as that of the 1
639 wt% Pt samples, two different sets of experiments were conducted. First, a screening test was
640 performed using 10 mM 5-HMF solutions and a 12 h irradiation period in the presence of 0.2
641 mg/ml of each catalyst. Subsequently, the top-performing catalyst from the screening was selected
642 and a second series of experiments designed to assess the influence of solvent composition and O_2
643 availability on activity and selectivity. Specifically, the H_2O content was varied from 100% to 20%
644 in MeCN and the atmosphere was altered from inert (Ar saturated) to O_2 -saturated, under a shorter
645 irradiation time of 6 hours. This strategy aimed to correlate water content and oxygen-dependent
646 reactive oxygen species (ROS) generation with catalytic activity. The conversion efficiency was
647 primarily monitored via UV-Vis spectroscopy, based on the depletion of the characteristic $\pi \rightarrow$
648 π^* transition absorption band of the 5-HMF furanic ring at 284 nm, while the liquid-phase products
649 were detected via HPLC. **Figure 7a, b** reveals the intrinsic photocatalytic oxidation ability of the
650 selected photocatalysts toward 5-HMF. The highest performance was achieved by the Cu-FDT_A
651 deNa catalyst, which attained 89.7% degradation of 5-HMF over 12 hours of irradiation,
652 corresponding to a degradation rate of $3.74 \text{ mmol}_{5\text{-HMF}} \cdot \text{g}^{-1} \cdot \text{h}^{-1}$. Notably, the addition of 1 wt% Pt
653 although beneficial for HER due to its role as a co-catalyst for electron extraction and
654 recombination suppression did not enhance the oxidative performance of either the sodium-rich or
655 the desodiated catalyst. This suggests that the improved charge separation facilitated by Pt does



not directly translate into a higher concentration of reactive h^+ available for 5-HMF oxidation. We propose that Pt nanoparticles may preferentially occupy surface sites crucial for the adsorption of 5-HMF, a critical initial step in its oxidation pathway. As a result, the reaction kinetics may become limited by substrate adsorption rather than charge carrier availability. Despite this, the Na-rich catalysts (Cu-FDT_A and 1 wt% Pt @ Cu-FDT_A) demonstrated significant activity, achieving 69.7% and 70% degradation, respectively. This result indicates a favorable interaction between surface sodium species and 5-HMF, potentially Brønsted-basic in character, through Na-O-bonding, that enhances the binding of 5-HMF through its aldehyde group and facilitates subsequent oxidation.⁷⁰⁻⁷² HPLC analysis revealed that photocatalytic oxidation of 5-HMF over the heterojunction catalysts resulted primarily in complete mineralization, as it can be concluded

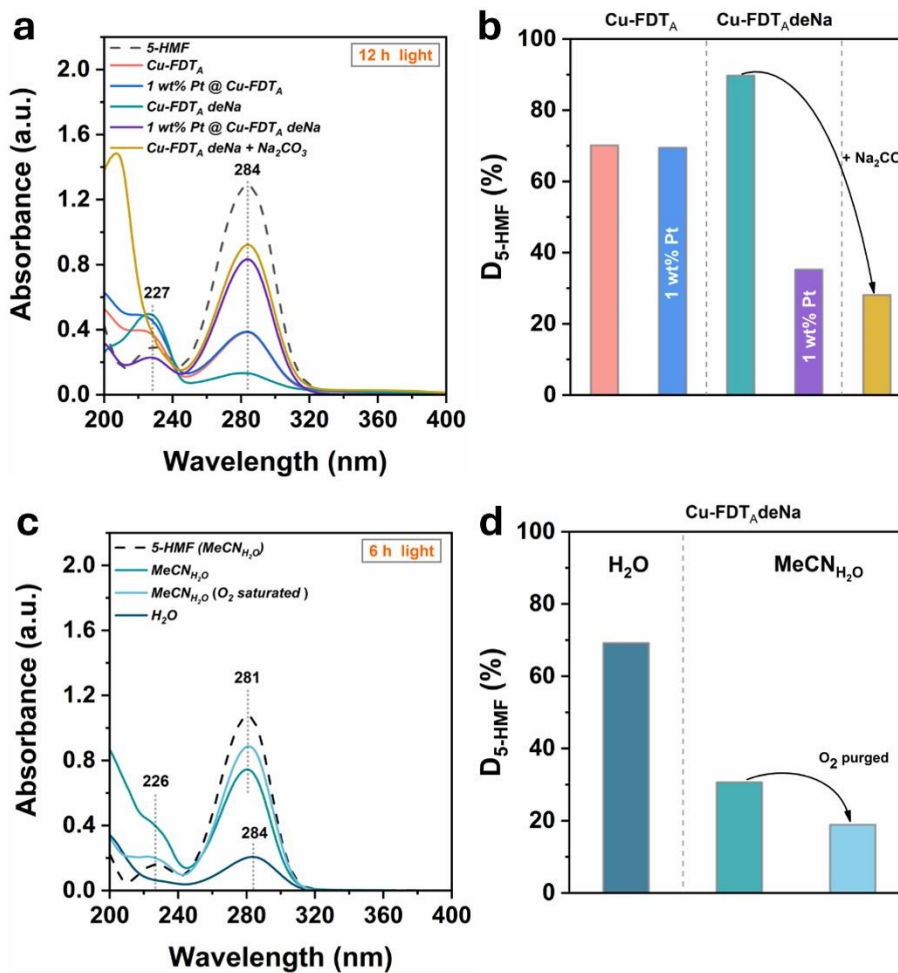


Figure 7. a) UV-Vis screening of the synthesized catalysts with 10 mM 5-HMF as substrate and scavenging with Na_2CO_3 for a reaction duration of 12 h. **b)** Degradation percentage of 5-HMF using selected photocatalysts for a reaction duration of 12 h. **c)** UV-Vis spectra of the reaction solutions employing Cu-FDT_A deNa with different reaction conditions and reaction duration of 6 h. **d)** Degradation percentage of 5-HMF in H_2O and MeCN 80% using 5 mg of Cu-FDT_A deNa, 10 mM 5-HMF and 6 h of light irradiation.

666 by the rise in the absorption at 226 - 227 nm arising from formic acid (FA) (**Figure S9 and Figure**
667 **7a**). Only trace intermediates, HMFCA and DFF, were detected with the sodium-rich Cu-
668 FDT/anatase heterojunctions and with the more active oxidative catalyst, Cu-FDTA deNa. This
669 high degree of mineralization is attributed to the strong adsorption of 5-HMF onto the catalyst
670 surface, coupled with the high oxidative potential of valence band- h^+ at Cu-FDT, which enables
671 deep oxidation (**Figure 6**).^{73,74} To probe the role of reactive species, Na_2CO_3 , a known h^+
672 scavenger was introduced, resulting in a sharp reduction of the 5-HMF degradation rate to 28%
673 using Cu-FDT_A deNa. This strong inhibition clearly confirms that photogenerated h^+ are the
674 dominant oxidative species driving 5-HMF oxidation (**Figure 7a, b**).⁷⁵ Furthermore, no shift of
675 the absorption peak of 5-HMF at 384 nm was observed, indicating a persistent hole-mediated
676 oxidation toward deep oxidation products rather than through a selective pathway.⁷⁶

677 The roles of solvent and O_2 in the photocatalytic reaction, were assessed by further testing
678 the top-performing Cu-FDT_A deNa heterojunction under controlled conditions (**Figure 7c, d**). In
679 pure aqueous medium and under Ar-saturated atmosphere, 69% degradation was achieved after 6
680 hours of irradiation, owing to the higher catalyst loading (**Figure 7d**). The high activity observed
681 in O_2 -deficient atmosphere supports the high participation of h^+ in the oxidation of 5-HMF,
682 alongside the pathway involving molecular O_2 -derived ROS such as the superoxide radical ($\cdot O_2^-$),
683 hydrogen peroxide (H_2O_2), hydroxyl radicals ($\cdot OH$) or singlet oxygen (1O_2). The importance of the
684 aqueous environment was further underscored by experiments performed in a mixed solvent
685 system ($MeCN_{H_2O}$, 80% v/v MeCN). A sharp drop in activity, resulting in only 31% degradation
686 was observed (**Figure 7d**). This drastic reduction can be attributed to two main factors, namely,
687 the decreased concentration of H_2O which contributes to ROS generation and the competitive
688 adsorption of MeCN onto the catalyst surface, which blocks active sites and hinders 5-HMF
689 adsorption.⁷³ Performing the reaction in O_2 -rich atmosphere further quenched the reaction rate.
690 This result suggests that O_2 competes with 5-HMF for photogenerated h^+ , rather than acting as an
691 e^- scavenger, thereby enhancing the oxidative performance of the photocatalyst.⁷⁷

693 Conclusions

694 Overall, the successful synthesis of a Cu-substituted Freudenbergite was demonstrated for
695 the first time, using a co-precipitation method. Comprehensive characterization-using PXRD,
696 XPS, STEM-EDS and HR-TEM-confirmed the formation of the material and the presence of Ti^{3+}
697 species for charge compensation. The band gap was estimated at 2.95 eV from UV-DRS using
698 the Kubelka-Munk method, while Mott-Schottky analysis revealed a Fermi band located at -0.25
699 V vs NHE (pH= 7). By adding a small amount of H_2O to the precursor solution prior to
700 precipitation, we achieved the *in-situ* fabrication of heterojunctions between Cu-FDT and TiO_2 .
701 The phase composition of TiO_2 (anatase, rutile) was controllably tuned by varying calcination
702 temperature. The presence of excess surface Na^+ was found to influence the stability and
703 thermodynamic phase transitions of TiO_2 as well as the stability of Cu-FDT. The photocatalytic
704 performance of the heterojunctions was evaluated for solar light driven HER using TEOA as a
705 sacrificial electron donor. The most active catalyst was the desodiated Cu-FDT/anatase



706 heterojunction (Cu-FDT_A deNa), which, when loaded with 1 wt% Pt, achieved a remarkable rate
707 of 7183 $\mu\text{molH}_2\cdot\text{g}^{-1}\cdot\text{h}^{-1}$. Photocatalytic experiments, transient photocurrent, EIS, and HER
708 polarization with Tafel analysis collectively elucidated the dual-phase influence of the excess
709 surface Na⁺ on the HER activity of the Cu-FDT/anatase heterojunction. PL quenching and Mott-
710 Schottky analysis indicated a direct Z-scheme charge transfer process, enabling utilization of the
711 highly reductive CB of anatase TiO₂ and the highly oxidative VB of Cu-FDT. Furthermore, the
712 Cu-FDTA deNa catalyst demonstrated excellent oxidative capability, achieving 89.7%
713 mineralization of 5-HMF after 12 hours of simulated solar-light irradiation, owing to the oxidative
714 power of photogenerated h⁺ on the VB of the Cu-FDT component. These findings establish Cu-
715 FDT-based heterojunctions as promising photocatalysts for simultaneous hydrogen production and
716 biomass-derived compound oxidation, opening new directions for solar-driven energy and
717 chemical conversion.

718

719 CRediT authorship contribution statement

720 P.T.: Writing-original draft, Conceptualization, Investigation, Formal Analysis, Data
721 Curation, and Visualization, E.S.: Investigation, L.K.: Data Curation, O.M.: Investigation,
722 N.B.: Resources, C.A.M.: Project Administration, Funding Acquisition, Supervision,
723 Resources, Writing – Review & Editing.

724

725 Conflicts of interest

726 There are no conflicts to declare.

727

728 Acknowledgements

729 This research has been co-funded by the Special Research Account of NKUA(No. 19712).
730 The authors would like to acknowledge Dr. Labrini Sygellou for conducting the X-Ray
731 photoelectron spectroscopy (XPS) measurements at the Surface Science Characterization
732 Laboratory in the Institute of Chemical Engineering Sciences, FORTH-ICEHT. All powder
733 diffraction data were collected in the National and Kapodistrian University of Athens X-Ray
734 Diffraction Core Facility. The assistance of MSc Maria Kourmousi with the electrochemical
735 impedance measurements is also gratefully acknowledged.

736

737 References

- 738 1 J. D. Burrington, *ACS Omega*, 2024, 9, 25841–25858.
- 739 2 M. Yue, H. Lambert, E. Pahon, R. Roche, S. Jemei and D. Hissel, *Renewable and Sustainable*
740 *Energy Reviews*, 2021, 146, 111180.



741 3 A. D. G. Kafadi, H. Y. Hafeez, J. Mohammed, C. E. Ndikilar, A. B. Suleiman, A. T. Isa and F. K.
742 Alharbi, *Eur J Inorg Chem*, 2025, 28, e202500191.

743 4 K. Maeda and K. Domen, *Journal of Physical Chemistry Letters*, 2010, 1, 2655–2661.

744 5 M. Mohsin, I. A. Bhatti, M. Zeshan, M. Yousaf and M. Iqbal, *Elsevier B.V.*, 2023, preprint, DOI:
745 10.1016/j.flatc.2023.100547.

746 6 P. Tzevelekidis, M. Theodosiou, A. Papadopoulou, E. Sakellis, N. Boukos, A. K. Bikogiannakis, G.
747 Kyriakou, E. K. Efthimiadou and C. A. Mitsopoulou, *Helyon*, 2024, 10, e35634.

748 7 S. Ahmetović, Z. Vasiljević, J. B. Krstić, M. Finšgar, D. Solonenko, D. Bartolić, N. B. Tadić, G.
749 Miskovic, N. Cvijetićanin and M. V. Nikolic, *Surfaces and Interfaces*, 2024, 49, 104434.

750 8 A. Chauhan, S. Agnihotri and M. Vasundhara, *Environmental Science and Pollution Research*,
751 2024, 31, 47991–48013.

752 9 L. Yang, C. Wang, Y. Li, W. Ge, L. Tang, J. Shen, Y. Zhu and C. Li, *Adv Funct Mater*, 2024, 34,
753 2401094.

754 10 L. T. Pérez-Poyatos, S. Morales-Torres, L. M. Pastrana-Martínez and F. J. Maldonado-Hódar, *Catal
755 Today*, 2025, 446, 115115.

756 11 L. Li, Y. Wang, Y. Ruan, T. Xu, S. Wu and W. Lu, *Appl Surf Sci*, 2024, 672, 160771.

757 12 L. Sui, W. Chen, X. Long, J. Liao, S. Wang and X. Wei, *Int J Hydrogen Energy*, 2024, 55, 855–863.

758 13 Z. Jiang, Z. Y. Zhang, W. Shangguan, M. A. Isaacs, L. J. Durndell, C. M. A. Parlett and A. F. Lee,
759 *Catal Sci Technol*, 2016, 6, 81–88.

760 14 P. Tzevelekidis, E. Sakellis, N. Boukos, A. K. Bikogiannakis, G. Kyriakou, J. Praxmair, G. A. Zickler, S.
761 Pokrant and C. A. Mitsopoulou, *J Mater Chem A Mater*, 2025, 13, 39859–39876.

762 15 C. Hu, Y. K. Jhao, Y. T. Chang, L. H. Kao, K. S. Chuang, J. H. Huang and A. Wibowo, *J Alloys Compd*,
763 2025, 1032, 181104.

764 16 Y. Liu, X. Zheng, Y. Yang, J. Li, W. Liu, Y. Shen and X. Tian, *ChemCatChem*, 2022, 14, e202101439.

765 17 B. Zhang, F. Liu, B. Sun, T. Gao and G. Zhou, *Chinese Journal of Catalysis*, 2024, 59, 334–345.

766 18 B. H. Xiao, C. Huo, J. Y. Chen, Y. G. Xiao, S. S. Cao and Z. Q. Liu, *Chem Sci*, 2025, 16, 4876–4883.

767 19 D. R. Eddy, M. D. Permana, L. K. Sakti, G. A. N. Sheha, G. A. N. Solihudin, S. Hidayat, T. Takei, N.
768 Kumada and I. Rahayu, *Nanomaterials*, 2023, 13, 704.

769 20 S. N. Kulkarni, R. Ragesh Nath, K. Alkanad, A. Amasegowda, S. C. Ke and N. K. Lokanath, *J Alloys
770 Compd*, 2025, 1016, 178876.

771 21 D. Li, R. Li, D. Zhou, X. Qin and W. Yan, *Fuel*, 2025, 388, 134237.

772 22 D. P. Opra, V. V. Zhelezov, S. L. Sinebryukhov, A. A. Sokolov, A. M. Ziatdinov, A. B. Podgorbunsky,
773 A. V. Gerasimenko, A. Y. Ustinov, V. G. Kuryavy, D. A. Saritsky, A. I. Neumoin, N. I. Zaytsev, N. V.
774 Polyakova and S. V. Gnedenkov, *J Power Sources*, DOI:10.1016/j.jpowsour.2024.234230.



775 23 C. Wu, Z. G. Wu, X. Zhang, R. Rajagopalan, B. Zhong, W. Xiang, M. Chen, H. Li, T. Chen, E. Wang, Z. Yang and X. Guo, *ACS Appl Mater Interfaces*, 2017, 9, 43596–43602.

777 24 P. Yang, L. Xu, Y. Tao, W. Wang, X. Wu and D. Zhang, *Journal of Electroanalytical Chemistry*, 2024, 954, 118051.

779 25 T. Ishiguro, K. Tanaka, F. Marumo, M. G. M. U. Ismail, S. Hirano and S. Sōmiya, *urn:issn:0567-7408*, 1978, 34, 255–256.

781 26 Z. Q. Guo, N. X. Miao, J. P. Zhou, Y. X. Lei, Q. U. Hassan and M. M. Zhou, *J Mater Chem A Mater*, 2017, 5, 17589–17600.

783 27 G. Bruhn, S. Beutel, G. Pfaff and B. Albert, *J Alloys Compd*, 2015, 644, 783–787.

784 28 E. Morgado, B. A. Marinkovic, P. M. Jardim, M. A. S. De Abreu, M. D. G. C. Rocha and P. Bargiela, *Mater Chem Phys*, 2011, 126, 118–127.

786 29 Q. W. Chen, Z. Q. Guo and J. P. Zhou, *Appl Surf Sci*, 2024, 648, 158689.

787 30 E. Morgado, B. A. Marinkovic, P. M. Jardim, M. A. S. De Abreu, M. D. G. C. Rocha and P. Bargiela, *Mater Chem Phys*, 2011, 126, 118–127.

789 31 R. G. Ciocarlan, E. M. Seftel, R. Gavrila, M. Sachea, M. Batuk, M. Mertens, J. Hadermann and P. Cool, *J Alloys Compd*, 2020, 820, 153403.

791 32 H. Tang, R. Yang and W. Gao, *Physica B Condens Matter*, 2018, 534, 120–124.

792 33 P. Umek, M. Pregelj, A. Gloter, P. Cevc, Z. Jaglicic, M. Čeh, U. Pirnat and D. Arčon, *Journal of Physical Chemistry C*, 2008, 112, 15311–15319.

794 34 A. B., J. A., A. S. Rao, S. S. Nagarkar, A. Dutta, S. P. Duttagupta, S. S. Prabhu and R. Pinto, *Int J Hydrogen Energy*, 2024, 81, 1442–1466.

796 35 M. Wang, H. Zhou and F. Wang, *Joule*, 2024, 8, 604–621.

797 36 X. Su, T. Xiao, Q. Gong, H. Cheng and F. Zhao, *Green Chemistry*, 2025, 27, 9846–9861.

798 37 X. Bao, M. Liu, Z. Wang, D. Dai, P. Wang, H. Cheng, Y. Liu, Z. Zheng, Y. Dai and B. Huang, *ACS Catal*, 2022, 12, 1919–1929.

800 38 W. Zhang, Q. Li and H. Xia, *Appl Surf Sci*, 2023, 613, 156036.

801 39 Z. Luo, Y. Zhu, Y. luo, G. Ren, Y. Wang and H. Tang, *Acta Physico-Chimica Sinica*, 2025, 100166.

802 40 F. Kamatsos, M. Drosou and C. A. Mitsopoulou, *Int J Hydrogen Energy*, 2021, 46, 19705–19716.

803 41 L. Shi, K. Chen, T. Huang, Y. Zhang, Z. Wang and Q. Zhang, *Ceram Int*, 2024, 50, 23937–23944.

804 42 M. Zhang, M. Liu, K. Han, Y. Liang, X. Zhao, L. Han, J. Wang, S. Wang and Y. Li, *Molecules* 2024, Vol. 29, Page 5385, 2024, 29, 5385.

806 43 R. G. Ciocarlan, E. M. Seftel, R. Gavrila, M. Sachea, M. Batuk, M. Mertens, J. Hadermann and P. Cool, *J Alloys Compd*, 2020, 820, 153403.



808 44 M. Hodos, E. Horváth, H. Haspel, Á. Kukovecz, Z. Kónya and I. Kiricsi, *Chem Phys Lett*, 2004, 399, 512–515.

809

810 45 V. D. Chinh, A. Broggi, L. Di Palma, M. Scarsella, G. Speranza, G. Vilardi and P. N. Thang, *J Electron Mater*, 2018, 47, 2215–2224.

811

812 46 H. Dai, W. Xu, K. Yu and W. Wei, *Chinese Chemical Letters*, 2019, 30, 517–520.

813 47 M. C. Biesinger, *Surface and Interface Analysis*, 2017, 49, 1325–1334.

814 48 S. Tsatsos and G. Kyriakou, *The Journal of Physical Chemistry C*, 2023, 127, 6337–6346.

815 49 Y. Bourlier, M. Bouttemy, O. Patard, P. Gamarra, S. Piotrowicz, J. Vigneron, R. Aubry, S. Delage and A. Etcheberry, *ECS Journal of Solid State Science and Technology*, 2018, 7, P329–P338.

816

817 50 L. H. C. Andrade, S. M. Lima, A. Novatski, A. M. Neto, A. C. Bento, M. L. Baesso, F. C. G. Gandra, Y. Guyot and G. Boulon, *Phys Rev B Condens Matter Mater Phys*, DOI:10.1103/PhysRevB.78.224202.

818

819 51 M. D. Roy, T. P. Gompa, S. M. Greer, N. Jiang, L. S. Nassar, A. Steiner, J. Bacsa, B. W. Stein and H. S. La Pierre, *J Am Chem Soc*, 2024, 146, 5560.

820

821 52 Y. Chen, X. Feng, Y. Liu, X. Guan, C. Burda and L. Guo, *ACS Energy Lett*, 2020, 5, 844–866.

822 53 Z. Zhang and J. T. Yates, *Chem Rev*, 2012, 112, 5520–5551.

823 54 A. J. . Bard and L. R. . Faulkner, *Electrochemical methods : fundamentals and applications*, John Wiley & Sons, Inc., 2001.

824

825 55 B. N. Cardoso, E. C. Kohlrausch, M. T. Laranjo, E. V. Benvenutti, N. M. Balzaretti, L. T. Arenas, M. J. L. Santos and T. M. H. Costa, *International Journal of Photoenergy*, 2019, 2019, 7183978.

826

827 56 M. Avdeev and V. B. Nalbandyan, *Inorg Chem*, 2006, 45, 2217–2220.

828 57 D. D. Eberl and J. Srodon, *American Mineralogist*, 1988, 73, 1335–1345.

829 58 G. C. C. Viana, D. L. S. Maia, D. A. S. Rodrigues, L. F. S. Ribeiro, I. O. Mazali, F. Rodrigues-Silva, M. C. V. M. Starling, T. A. Neves and C. C. Amorim, *Journal of Water Process Engineering*, 2025, 77, 108441.

830

831

832 59 Q. Li, C. Wang, H. Yao, C. He, C. Guo and Y. Hu, *Coord Chem Rev*, 2025, 535, 216652.

833 60 L. Xie, P. Wu, Q. Lei, C. Xu, W. Huang, X. Chen, K. Yang and H. He, *Catalysts*, 2023, 13, 583.

834 61 T. Ano, F. Kishimoto, S. Tsubaki, Y. H. Lu, J. N. Hohman, M. M. Maitani, M. Salmeron and Y. Wada, *The Journal of Physical Chemistry C*, 2021, 125, 13984–13989.

835

836 62 A. Molinari, A. Maldotti and R. Amadelli, *Catal Today*, 2017, 281, 71–77.

837 63 V. Pfeifer, P. Erhart, S. Li, K. Rachut, J. Morasch, J. Brötz, P. Reckers, T. Mayer, S. Rühle, A. Zaban, I. Mora Seró, J. Bisquert, W. Jaegermann and A. Klein, *Journal of Physical Chemistry Letters*, 2013, 4, 4182–4187.

838

839

840 64 X. Li, J. Yu, J. Low, Y. Fang, J. Xiao and X. Chen, *J Mater Chem A Mater*, 2015, 3, 2485–2534.



841 65 W. Zhao, W. Ma, C. Chen, J. Zhao and Z. Shuai, *J Am Chem Soc*, 2004, 126, 4782–4783.

842 66 B. Liu, X. Liu, J. Liu, C. Feng, Z. Li, C. Li, Y. Gong, L. Pan, S. Xu and C. Q. Sun, *Appl Catal B*, 2018, 226, 234–241.

844 67 L. Ma, S. Liu, J. Xu, N. Zhao, S. Li, W. Jiang, Z. Pan, B. Yang, Y. Liu and B. Lai, *J Environ Manage*, 2025, 391, 126674.

846 68 P. Vernoux, A. Y. Leinekugel-Le-Cocq and F. Gaillard, *J Catal*, 2003, 219, 247–257.

847 69 I. V. Yentekakis, G. Moggridge, C. G. Vayenas and R. M. Lambert, *J Catal*, 1994, 146, 292–305.

848 70 L. Chico-Mesa, A. Rodes, R. M. Arán-Ais and E. Herrero, *Nature Communications*, 2025, 16, 1–11.

849 71 S. Li, M. Dong, J. Yang, X. Cheng, X. Shen, S. Liu, Z. Q. Wang, X. Q. Gong, H. Liu and B. Han, *Nat Commun*, 2021, 12, 584.

851 72 A. Ulyankina, S. Mitchenko and N. Smirnova, *Processes*, DOI:10.3390/pr8060647.

852 73 U. I. Gaya and A. H. Abdullah, *Journal of Photochemistry and Photobiology C: Photochemistry Reviews*, 2008, 9, 1–12.

854 74 S. Yurdakal, B. S. Tek, O. Alagöz, V. Augugliaro, V. Loddo, G. Palmisano and L. Palmisano, *ACS Sustain Chem Eng*, 2013, 1, 456–461.

856 75 B. Zhou, J. Song, Z. Zhang, Z. Jiang, P. Zhang and B. Han, *Green Chemistry*, 2017, 19, 1075–1081.

857 76 N. Cascelli, V. Gotor-Fernández, I. Lavandera, G. Sannia and V. Lettera, *Int J Mol Sci*, DOI:10.3390/ijms242316861.

859 77 J. B. G. Filho, I. F. Silva, M. Alafandi and J. Rabeah, *Molecules*, 2023, 28, 8077.

860



Highly active Cu-Freudenbergite/TiO₂ Heterojunction for Solar-driven Hydrogen Evolution and 5-Hydroxymethylfurfural oxidation.

Panagiotis Tzevelekidis,^a Elias Sakellis,^{b, c} Loukas Koutsokeras,^c Olga Martzoukou,^d Nikos Boukos,^b and Christina A. Mitsopoulou^{*a}

^a Inorganic Chemistry Laboratory, Department of Chemistry, National and Kapodistrian University of Athens 15771 Zografou, Greece

^b Institute of Nanoscience and Nanotechnology, National Centre of Scientific Research “Demokritos”, Agia Paraskevi, 15341, Greece

^c Section of Condensed Matter Physics, Department of Physics, National and Kapodistrian University of Athens, Athens, 15784, Greece

^d Enzyme and Microbial Biotechnology Unit, Department of Biology, National and Kapodistrian University of Athens, Athens, 15784, Greece

Data availability

The data supporting this article have been included as part of the Supplementary Information

